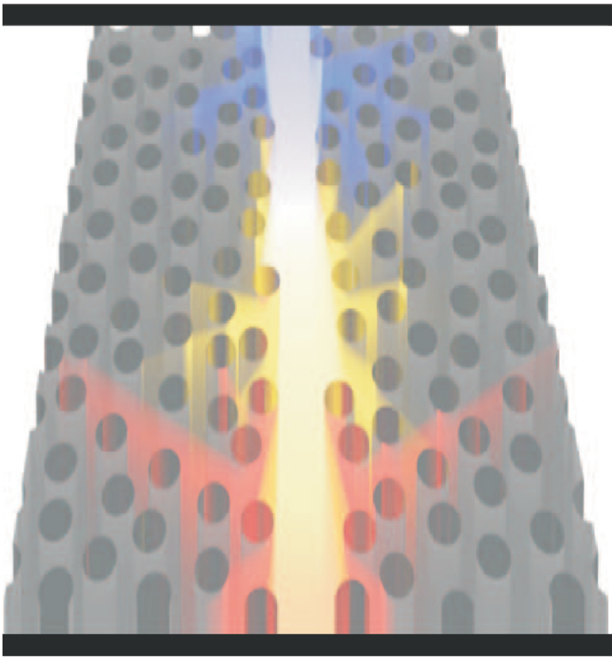

Semiconductor Nanomembranes for Quantum Photonics: Quantum Light Sources and Optomechanics

Jin Liu
Ph.D. Thesis
July 2012

DTU Fotonik
Department of Photonics Engineering

Semiconductor Nanomembranes for Quantum Photonics: Quantum Light Sources and Optomechanics

A dissertation
submitted to the Department of Photonics Engineering
at the Technical University of Denmark
in partial fulfillment of the requirements
for the degree of
philosophiae doctor

Jin Liu
July 15, 2012

Semiconductor Nanomembranes for Quantum Photonics: Quantum Light Sources and Optomechanics

Preface

The research presented in this thesis has been carried out in Quantum Photonics Group, DTU Fotonik at the Technical University of Denmark from July 2009 to July 2012 while I was enrolled as a Ph.D. student. The work has been carried out under the supervision of Professor Peter Lodahl and Professor Jesper Mørk.

First of all, I would like to thank my main supervisor Peter Lodahl for guidance and directing my research in interesting directions. I would also like to thank Jesper Mørk for coordinating a cluster with unique and broad set of competences in fabrication, optics and theory for doing research here.

A lot of people have contributed to the work presented here. First of all I would like to thank Søren Stobbe for the daily supervisions. I am also grateful to Henri Nielsen for introducing me to the laboratory and Serkan Ates for a lot of help and teaching me many tricks in the laboratory. I especially appreciate the insight from David Garcia on random lasing, which makes this work sharp at the end of my Ph.D. period. Furthermore, I would like to thank Martin Schubert for the help in Femto-lab, Sara Ek for fabrication of the samples used for random lasing, Niels Gregersen, Troels Skovgård and Michael Lorke for the modeling of nanolasers. I enjoyed the collaborations with people in NBI with whom we did a wonderful project on GaAs optomechanics. They are Koji Usami, Andreas Næsby, Tolga Bagci and Eugene Polzik.

A special thank goes to the people with whom I shared office with: David, Kristian, Immo, Henri, Stephan, Mads and Mikkel for good discussions and fun, making my time at DTU and later at NBI enjoyable. I would like to thank everyone in Quantum Photoincs Group for making it a pleasant place to work.

Finally I would like to thank to my family and my girl friend Qianqian for the support.

Abstract

This thesis describes the fabrication and characterizations of semiconductor nanomembranes, i.e., gallium arsenide (GaAs) photonic crystal (PC) and optomechanical nanomemebranes.

Processing techniques are developed and optimized in order to fabricate PC membranes for quantum light sources and optomechanical nanomembranes for cavity cooling experiments. For PC cavities, several important processes have been extensively optimized such as the inductively coupled plasma (ICP) dry etch, the release of the membranes and the post-cleaning of the samples. GaAs optomechanical nanomembranes with a world-record mechanical Q-factor up to 1 million have been fabricated with two step selective wet etches. These optomechanical naonmembranes exhibit superb performances in cavity optomechanical cooling experiments in which a mechanical mode has been cooled from room temperature to 4 K.

The interaction between single quantum dots (QDs) and PC cavities has been modeled in the framework of Jaynes-Cummings model (JCM) with the focus on single artificial atom lasers. In the experiments, a highly efficient single photon source with a collection efficiency up to 38% has been achieved and detailed measurements suggest that such a high efficiency could be attributed to the coupling to one of the higher-order cavity modes. Lasing oscillation has also been observed in the same systems. The comparison between the experimental lasing data to an advanced theory reveals that QDs lasing is fundamentally different from single atoms lasing due to the mesoscopic features of QDs.

Random lasers in Anderson-localization regime have been achieved in PC waveguides where the laser output can be controlled with the underlying dispersion relation. The random lasers can be well fitted with a modified semiconductor laser rate equation, showing high-β factors and low mode volumes. The

statistical measurements provide a complete and coherent picture of the mechanism and physical properties of a random laser in the Anderson-localization regime which paves the way to control and optimize random lasing in low dimensional optical nanostructures commonly used for tailoring the light-matter interaction.

Resumé

Denne afhandling omhandler fabrikation og karakterisering af halvleder nanomembraner, navnlig fotoniske krystaller (PC) og optomekaniske nanomembraner i gallium arsenide (GaAs).

Produktionsteknikker er udviklet og optimeret med henblik på at fabrikere PC membraner til brug for kvantelyskilder og optomekaniske membraner til brug for eksperimenter om kavitets køling. For fabrikation af PC kaviteter er flere vigtige processer blevet udførligt optimeret, eksempelvis ICP tør ætsningen, frigørelsen af membranerne og den efterfølgende rensning af prøven. Optomekaniske nanomembraner i GaAs er blevet fabrikeret med en rekordhøj Q-faktor på op til en million ved hjælp af en to-trins selektiv våd ætsning. Disse optomekaniske nanomembraner udviser uovertrufne egenskaber i eksperimenter om optomekanisk kavitets køling, hvor en mekanisk tilstand er blevet kølet fra stuetemperatur ned til 4 K.

Vekselvirkningen mellem individuelle kvantepunkter (QDs) og PC kaviteter er beskrevet vha. Jaynes-Cummings modellen (JCM) med fokus på lasere baseret på enkelte kunstige atomer. I eksperimenterne er en meget effektiv enkelt fotonkilde med en opsamlings effektivitet på 38

Lasere baseret på uorden i Anderson-lokaliserings regimet er demonstrerede i PC bølgeledere, hvor laser udgangseffekten kan kontrolleres vha. den underliggende dispersions relation. Lasere baseret på uorden kan beskrives godt med en modificeret halvleder laser rate ligning, der viser høje beta faktorer og små tilstands volumener. Statiske målinger giver et komplet og sammenhængende billede af mekanismen og de fysiske egenskaber af en laser baseret på uorden i Anderson-lokaliserings regimet, hvilket baner vejen for at kontrollere og optimere lasere baseret på uorden i lav dimensionselle optiske nanostrukturer, der ofte bruges til at designe lys-stof vekselvirkningen.

List of Publications

The work performed in the work of this Ph.D.-project has resulted in the publications listed below:

Journal Publications

1. J. Liu, K. Usami, A.Naesby, T. Bagci, E. S. Polzik, P. Lodahl and S. Stobbe, *High-Q optomechanical GaAs nanomembranes*, Applied Physics Letters, **99**, 243102 (2011).

2. K. Usami, A.Naesby, T. Bagci, B. M. Nielsen, J. Liu, S. Stobbe, P. Lodahl and E. S. Polzik *Optical cooling of mechanical modes of a semiconductor naonmembrane*, Nature Physics, **8**, 168 (2012).

Journal Publications in Preparation

1. J. Liu, P. D. Garcia, N. Gregensen, M. Schubert, J. Mørk, S. Stobbe and P. Lodahl, *Statistical properties of random lasing in the Anderson-localization regime*, In preparation.

2. J. Liu, S. Ates, M. Lorke, S. Stobbe and P. Lodahl, *Few quantum dots laser in photonic crystal naoncavities*, In preparation.

Conference Contributions

1. J. Liu, S. Ates, M. Lorke, S. Stobbe and P. Lodahl, *Few quantum dots laser in photonic crystal naoncavities*, CLEO/Europe-EQEC Conference, Munich, Germany (2011).

2. A.Naesby, K. Usami, T. Bagci, B. M. Nielson, J. Liu, S. Stobbe, P. Lodahl and E. S. Polzik, *Optoelectronic cooling of mechanical modes in a semiconductor nanomembrane*, CLEO/Europe-EQEC Conference, Munich, Germany (2011).

Contents

Preface ii

Abstract iv

Resumé vii

List of publications viii

1 Introduction 1

2 Fabrication of photonic crystal and optomechanical nanomembranes 5

- 2.1 photonic crystal membranes 5
  - 2.1.1 Introduction 5
  - 2.1.2 E-beam lithography of photonic crystal patterns 8
  - 2.1.3 Dry etch of GaAs photonic crystals 8
  - 2.1.4 Release of the free-standing membrane structures 15
  - 2.1.5 Post-cleaning of the sample 20
- 2.2 High-Q GaAs optomechanical nanomembranes 22
  - 2.2.1 Introduction 22
  - 2.2.2 Fabrication of High-Q GaAs optomechanical nanomembranes 23
  - 2.2.3 Characterizations of GaAs optomechanical nanomembranes 28
  - 2.2.4 Applications of the GaAs optomechanical nanomembranes 32
- 2.3 Fabrication of wedged plasmonic waveguides 33
- 2.4 Conclusion and outlook 35

3 Highly efficient single-photon emission and lasing in photonic crystal nanocavities 37
3.1 Introduction . . . 38
3.1.1 Semiconductor quantum dots . . . 38
3.1.2 photonic crystal cavities . . . 39
3.2 Modeling single quantum dots in photonic crystal cavities . . . 41
3.2.1 Jaynes-Cummings model . . . 41
3.2.2 Jaynes-Cummings model with dissipations . . . 42
3.2.3 Modeling of a single artificial atom laser . . . 43
3.3 A highly efficient single-photon source . . . 48
3.4 Few quantum dots lasing in photonic crystal nanocavities . . . 54
3.5 Conclusion and outlook . . . 58
4 Anderson-localized random lasing 61
4.1 Introduction . . . 61
4.1.1 Multiple scattering of light . . . 61
4.1.2 Random lasing . . . 62
4.1.3 Anderson-localization of light in photonic crystal waveguides . . . 64
4.2 Random lasing in photonic crystal waveguides . . . 65
4.2.1 Sample characterizations . . . 65
4.2.2 Single- and multi-modes random lasing . . . 66
4.2.3 Modeling Random lasing . . . 68
4.2.4 Controlling light localization with gain . . . 71
4.3 Conclusion and outlook . . . 74
5 Conclusion 75
Appendices 77
A Fabrication procudures 79
A.1 PC membranes process . . . 79
A.2 GaAs optomechanical nanomembrane process . . . 80
A.3 Wedged plasmonic waveguides prcess . . . 81

B Detailed information on random lasers **83**
B.1 Sample fabrication 83
B.2 Experimental setup and optical characterizations 83
B.3 Rate equation analysis 84

C Optical characterization setup **89**

Bibliography **91**

Chapter 1

Introduction

With the advance of semiconductor nanofabrication techniques, high-quality, single-crystal and light-emitting semiconductor nanomembranes become available and serve as an ideal research platform for nanoscale light-matter interaction in a solid-state environment. They distinct from films due to their free-standing form which makes them isolated from the substrate. In low-dimensional semiconductor nanostructures, e.g., semiconductor nanomembranes light-matter interaction can be tailored with deliberately designed photonic and phononic nanostructures.

In 1946, Purcell proposed that spontaneous emission is a controllable process instead of an internal property of the emitter[1]. In the past decades, significant progresses on controlling spontaneous emission have been made in various systems with the advance of modern semiconductor technologies[2, 3, 4, 5]. The requirement of both very high-quality quantum emitters and a controllable optical environment is not easy to satisfy. Semiconductor nanomembranes provide an opportunity of engineering spontaneous and stimulated emission processes due to two advantages. First, molecular beam epitaxy (MBE) growth enables ideal solid-state quantum emitters, QDs, which are internally embedded into the semiconductor nanomembranes. Second, the recent progress in semiconductor nanofabrication makes it possible to fabricate sophisticated nanostructures like PC in which the optical density of the state (DOS) can be modified in a controllable way. A main focus of this thesis is the investigation of spontaneous and stimulated processes in varied structured semiconductor nanomembranes.

Utilizing ordered nanostructures such as PCs to enhance light-matter interaction has attracted tremendous research interests during past decades[6]. However, imperfections due the the fabrication process lead to random multiple scattering and, ultimately, to Anderson-localization of light[7]. The strongly localized modes induced by light localization offers an alternative route in which the light in confined at nanoscale by utilizing the disorder in the system. Another contribution of this thesis is the demonstration of random lasing in Anderson-Localization regime.

The mechanical force is an important aspect of light-matter interaction and it results in a prosper research field of optical trapping of nanoparticles and atoms (The optical trapping of atoms was awarded as a Nobel Price). Over the past few years, impressive progresses have been made in studying nano- and micromechanical resonators with the common aim of exploring the quantum regime of mechanical systems[8]. Semiconductor nanomembranes are particularly interesting because they could bring brand new mechanisms of cavity optomechanical cooling due to advantageous properties of direct band gap semiconductors. In this thesis, we will focus on the fabrication and characterizations of GaAs optomechanical nanomembranes which is one of the most promising candidates for the cooling of a mechanical resonator to its ground quantum state.

The outline of the thesis is as follows:

In chapter 2, the prerequisites of experimentally realizing the enhancement of light-matter interaction are the semiconductor nanomembranes with engineered photonic and phononic properties. Fabrication technologies have been developed to realize PC and optomechanical nanomembranes. Also, a selective wet etch process for wedged plasmonic waveguides has been developed. All the structures fabricated in the course of this work are presented along with their fabrication procedures in this chapter. Highlights of some of the experiments performed on the optomechanical nanomembranes are discussed.

Investigations of single-photon emission and nanolasers based on QDs in semiconductor PC membranes are presented in Chapter 3. A single-photon source with a collection efficiency of 38% after first collection lens has been experimentally achieved with a quasi-resonant excitation scheme. The photon statistics measurement show perfect anti-bunching, which is the signature of single-photon emission. The prerequisites of a single artificial atom laser have been theoretically investigated based on Jaynes-Cummings model (JCM). We further examine the influence of pure dephasing on the lasing within the frame of JCM. In the experiments, we have realized few QDs PC cavity nanolasers. By comparing our experimental data to an advanced semiconductor micro-cavity laser model, we find that the multi-exciton states play an important role in QDs nanolasers.

Chapter 4 presents a realization of random lasing with Anderson-localized modes in PC waveguides. Our random lasers exhibit typical micro-cavity laser characteristics such as high-β factors and low mode volumes. The random lasing has been modeled with a modified semiconductor laser rate equation. We get a very good agreement between the experimental data and our model. The statistical measurement of random lasers reveals its underlying physical mechanism and important physical properties.

Finally, conclusions and an outlook are presented in Chapter 5.

Chapter 2

Fabrication of photonic crystal and optomechanical nanomembranes

This chapter describes the samples fabricated in the course of this project with particular emphasis on crucial technical details to minimize the fabrication imperfections and with highlights from the measurements performed on GaAs optomechanical nanomembranes. All of the processing is done in Danchip which is the cleanroom facility at Technical University of Denmark (DTU). The fabricated samples can be divided in two categories: PC membranes and optomechanical nanomembranes. The details of their fabrications along with the realization of wedged plasmonic waveguides are discussed in the following. The developed fabrication recipes are included in Appendix A.

2.1 photonic crystal membranes

2.1.1 Introduction

PCs are nanostructures with periodic subwavelength modulation of the refractive index. This effect has been observed in naturally occurring opals and butterfly wings[9], etc. and is known as structural colors as opposed to pigment colors. PCs can be traced back to 1987 when E. Yablonovitch[10] and S. John[11] independently proposed this idea. The former is focused on controlling spontaneous emission with a photonic band gap analogous to the electronic band gap in semiconductors in three-dimensional PC structures, which is related the work presented in Chapter 3, while the latter is associated to the light localization at the band-edge where the optical DOS is high, which serves as the underlying physics of the work presented in Chapter 4. Although only three-dimensional PCs exhibit complete photonic band gaps it turns out that suspended membrane structures with periodic air holes can also confine light in three-dimensions. In this case the light is localized in-plane by the two-dimensional photonic band gap and confined vertically by total internal reflection.

One of the most important advantages of PC membranes over three-dimensional structures is that their fabrication process is directly compatible with existing planar semiconductor technology and the patterns of PCs can be very well defined by electron beam (e-beam) lithography. Presently, the PC membranes structure made by silicon show superb optical properties. For instance, the quality factor, Q, measured with a silicon PC cavity is as high as 1.3 million[12]. Silicon is the commercially most important semiconductor because they are cheap and easy to etch. On the other hand, the indirect band gap make it almost impossible to make active optoelectronic devices with silicon. The III-V material exhibits many advantages over silicon, e.g., direct electronic band gap, the advanced technology for III-V heterostructure growth by epitaxy method including the availability of high-quality QDs, significant piezoelectric effects. The GaAs PC membranes embedded with high-quality quantum emitter, indium arsenide (InAs) QDs, provide an ideal testbed for controlling the spontaneous and stimulated emission.

The semiconductor heterostructures used for the fabrication of PC membranes are grown on a (100)-oriented semi-insulating GaAs substrate by molecular beam epitaxy (MBE). The structure consists of a 160-nm-thick GaAs membrane, which was grown on a 1000-nm-thick AlGaAs sacrificial layer, incorporating 1 layer of InAs QDs at the center. Wafers with the same layer structure but without QDs have also been used to make passive PC membranes and optomechanical nanomembranes. We refer the wafer with QDs grown by MBE as 'active' wafers while those without QDs by metal organic chemical vapor

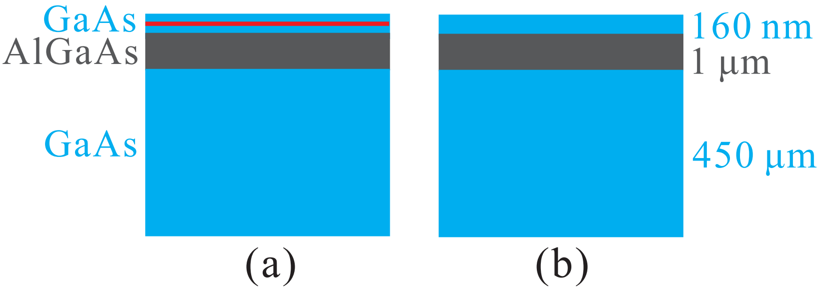

Figure 2.1: Sketches of the wafers used in the fabrication. (a) Sketch of an 'active' wafer. (b) Sketch of a 'passive' wafer. The blue layer represents GaAs material and the dark layer show the AlGaAs layer. The red line represents a QDs layer sitting in the center of the GaAs membrane layer.

deposition (MOCVD) as 'passive' wafers, as shown in Fig. 2.1.

In this chapter, we will go through the whole process development and discuss a few techniques used in the process for improving the device performance. A schematic overview of the PC membranes fabrication process is shown in Fig. 2.2. The PC patterns are firstly defined with e-beam lithography in an e-beam resist and then transferred into GaAs layers by dry etch and finally a wet etch is used to release the membranes.

For the pattern-transfer into the GaAs, we develope a process based on inductively-coupled plasma (ICP)[13] etching by using an e-beam resist as the dry etch masks instead of employing SiO_2 hard masks. By doing so, we greatly reduce the fabrication complexity and increase the reproducibility of the process.

Underetch of the sacrificial layer to release the free-standing membranes is not a trivial task and it could limit the final device performance without very careful processing. We find that high-quality free-standing membrane structures are very hard to be obtained for the 'passive' wafer by using a standard wet etch which works very well for the 'active' wafer. We will show how to overcome this obstacle by using a technique called vapor phase etch.

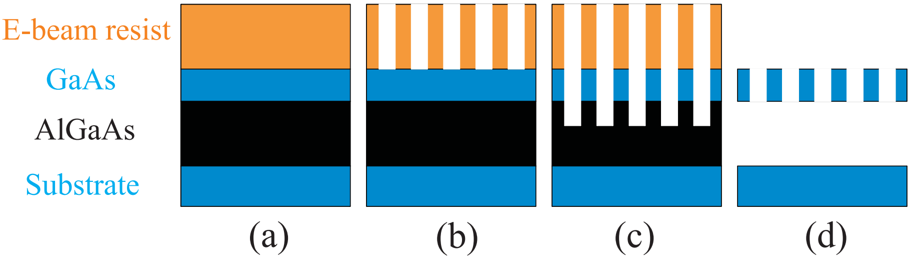

Figure 2.2: Schematic overview of the fabrication process for GaAs PC membranes.

2.1.2 E-beam lithography of photonic crystal patterns

A 500 nm ZEP 520A e-beam resist is spun on top of the GaAs layer. PC patterns are defined in the e-beam resist by using a 100 kV JEOL-9300FS e-beam lithography system. A two minutes over exposure is used after the e-beam process in order to make the holes round due to the proximity effect. The e-beam dose has been optimized with different doses for a large arrays of test samples in order to get vertical holes in the resist. Fig. 2.3(a) shows a typical dose optimized scanning electron microscope (SEM) picture of the e-beam resist after development. We found that the holes are uniformly defined with vertical sidewalls, which provides a good basis to transform the patterns into GaAs layer.

2.1.3 Dry etch of GaAs photonic crystals

We started out with the process by depositing a hard mask with a thickness of 160 nm SiO_2 on top of the wafer in a plasma-enhanced chemical vapor deposition (PECVD) reactor. On top of the hard mask e-beam resist is spun. PCs patterns defined in e-beam resist are normally transferred into a SiO_2 hard mask before the final etch into the PC membranes. The thin hard mask has a high etch selectivity which prevents the erosion of the soft e-beam resist and ensure the high resolution during the final etch in GaAs membranes. A fabrication process had previously been developed at Danchip to transfer PC patterns from a SiO_2 mask into GaAs by reactive ion etching (RIE) with methane/hydrogen (CH_4/H_2) plasma. A typical SEM image of the hole etched by an optimized RIE recipe based on hard masks is shown in Fig. 2.3(b) in

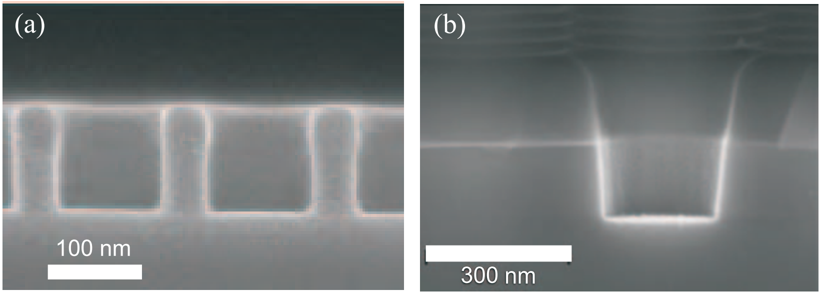

Figure 2.3: (a) SEM image of the e-beam resist exposed by an optimized dose after the development. (b) SEM image of the hole etched by an optimized recipe based on conventional RIE.

which the hole sidewalls are smooth but tend to exhibit sloped sidewalls. We realize that the low quality etch result by RIE process is limited by the inherent RIE technology instead of the dry etch recipe after a long-time process development. Hence we decide to adopt an inductively coupled plasma RIE (ICP) process. At the second year of my Ph.D. study, a new ICP etcher was installed in DTU Danchip. Compare to the RIE, ICP system can produce a much higher-density plasma that enhances the GaAs etch rate relative to the resist, which offers a possibility of doing the dry etch directly with an e-beam mask. One of the main drawbacks of the process with hard mask is the low reproducibility due to the extra PECVD and RIE processes.

ICP is a more advanced dry etch technology over conventional RIE. In the conventional RIE, a radio frequency (RF) plasma is generated by the electrode as shown in Fig. 2.4(a). The sample sits on top of the grounded electrode plate. Different gases needed in the dry etch are provided from pipes connected to chemical sources. The flow rates of gases and the chamber pressure are accurately controlled with valves and a vacuum pump. The gas molecules are dissociated into electrons, ions and reactive radicals under the RF field. The electrons absorbed by the earthed chamber wall flow to ground while those absorbed by the DC isolated electrode cannot flow away, which builds up a charge. The heavier ions then get accelerated to the electrode under the negative charge built in the electrode. The etch process is controlled physically by the ions sputtering into the electrode and chemically by the reactive radical. The physical sputtering tends to give rise to directional features while the

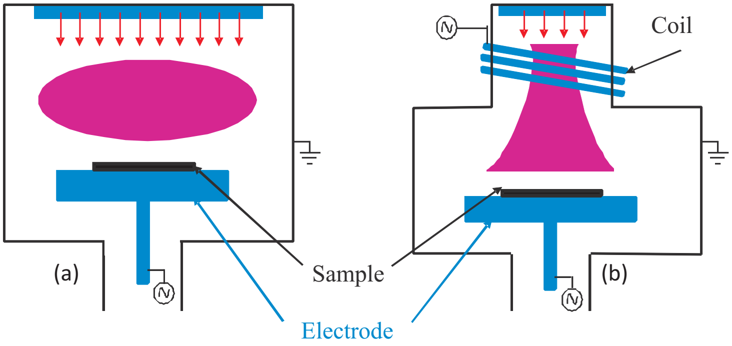

Figure 2.4: Schematic diagrams of the operation of RIE (a) and ICP (b). The purple shapes represent the confinement of the plasma. The red arrows show the input of the gas.

chemical reaction prefers to an isotropic etching. The final etching result is a balance between the physical part and the chemical part. The main problem of using RIE to fabricate PCs is the fact that no independent control over the degree of the dissociation of the plasma and the acceleration voltage can be obtained. ICP is such a solution in which a separate coil is introduced to produce the plasma, as shown in Fig. 2.4(b). In an ICP, the dissociation is determined by the coil RF power while the physical sputtering is controlled by the RF power on the electrode.

We start with an ICP recipe published by Kevin Hennessy et al.[14, 15] who have made very similar devices to our purpose by using ICP. Since the chamber condition can vary from machine to machine, the machine performance can also vary from company to company. Our final recipe could be very different from this initial recipe. Our start dry etch recipe is: 12 standard cubic centimeter per minute (sccm) Ar, 4 sccm Cl_2, 3 sccm BCl_3, 2.4 mTorr chamber pressure, 80 W platen power, 700 W coil power and 120 s etch time. The results are shown in Fig. 2.5(a). We find that the e-beam resist is almost gone while the holes have not reached the AlGaAs layer, which indicates that both etch rate and selectivity should be improved. On the other hand, the profile of the air hole looks smooth and close to vertical, which suggests that the chemical gas we chose in our process might be right and the platen power and coil power are not far from the target. It is very hard to decide which ICP parameter should be changed at this time because many machine parameters can influence the

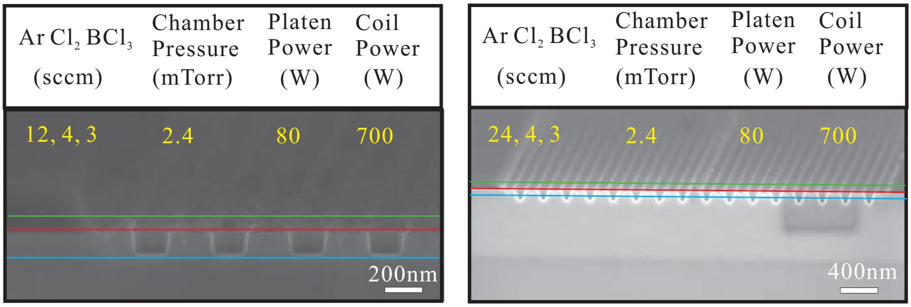

(a) (b)

Figure 2.5: SEM images of the holes etched by the start recipe (a) and the modified recipe (b) with 24 sccm Ar flow. Green line:interface between e-beam resist and air. Red line:interface between e-beam resist and GaAs layer. Blue line:interface between GaAs and AlGaAs layer.

etch rate and selectivity and these parameters are not independent.

The etching rate could be increased with more physical bombard in the dry etch, which can be realized by increasing the flow of Ar. In Fig. 2.5(b) a dry etch result with an Ar flow of 24 sccm is shown and a very tilted hole profile is obtained since the physical sputtering process is too strong due to such a high Ar flow.

The chamber pressure is one of the most important process parameters. It controls how much gas will be dissociated into electrons, ions and reactive radicals in the process. If the dry etching is mainly dominated by chemical process, higher etching rate is expected when increasing the chamber pressure due to the increasing chemical elements. On the contrary, the etching rate firstly increases and then slowly decreases if the etching is dominated by the physical process. In this case, the firstly increasing etching rate is due to the increasing number of the ions sputtering into the sample. The ion sputtering process become weak due to the collisions between ions under a very high chamber pressure, which results in a reduced etching rate.

Judging from the SEM image of our start recipe, we conclude both physical sputtering and chemical reaction play important roles in the process so we increase the chamber pressure in a systematic way in the second round dry etch test, which is presented in Fig. 2.6. From 6 mTorr to 20 mTorr we see the

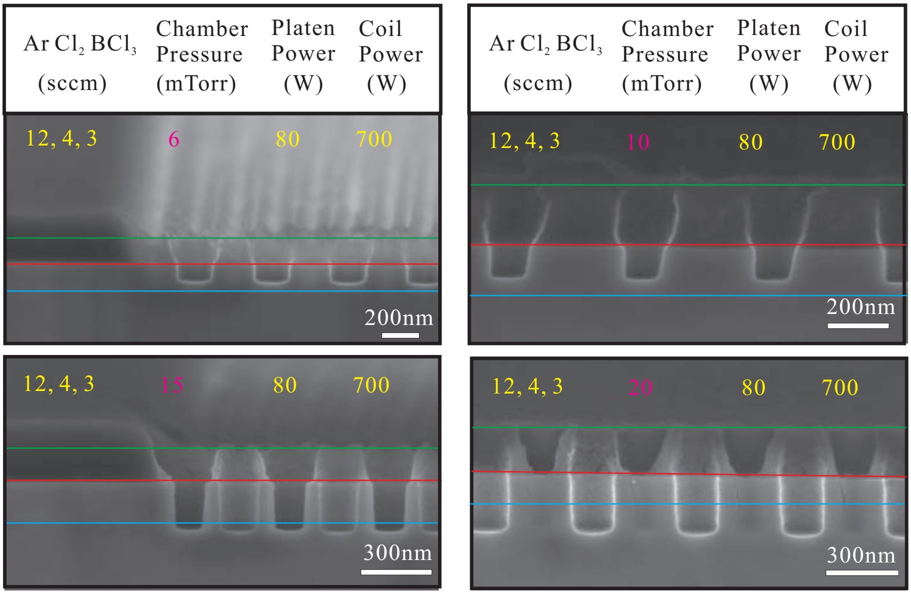
Ar Cl2 BCl3 (sccm)
Chamber Pressure (mTorr)
Platen Power (W)
Coil Power (W)
Ar Cl2 BCl3 (sccm)
Chamber Pressure (mTorr)
Platen Power (W)
Coil Power (W)
12, 4, 3
6
80
700
200nm
12, 4, 3
10
80
700
200nm
12, 4, 3
15
80
700
300nm
12, 4, 3
20
80
700
300nm

Figure 2.6: SEM image of the holes etched by recipes with different chamber pressures. The chamber pressure is varied from 6 to 20 mTorr. Green line:interface between e-beam resist and air. Red line:interface between e-beam resist and GaAs layer. Blue line:interface between GaAs and AlGaAs layer.

holes get deeper and deeper with the increasing chamber pressure and finally reached the sacrificial layer when the chamber pressure is up to 15 mTorr. At the same time, the e-beam resist left from dry etching gets thicker and thicker with increasing chamber pressure, which shows an enhanced selectivity for a higher pressure. The enhanced selectivity also suggests that the chemical process might dominates the dry etch process otherwise the selectivity would be decreased with the chamber pressure if it is mainly determined by the physical sputtering process in the dry etch.

By increasing the chamber pressure, we get holes with fairly good verticality and smoothness. In order to further optimize the dry etch recipe and understand the dry etch process, we have varied the platen power and coil power in a systematic way in the third round of the dry etch test. Fig. 2.7 shows the dry etch results with varied platen power ranging from 40 W to 100 W. The profiles of the holes look bowed for the low platen powers (40 W and 60 W)

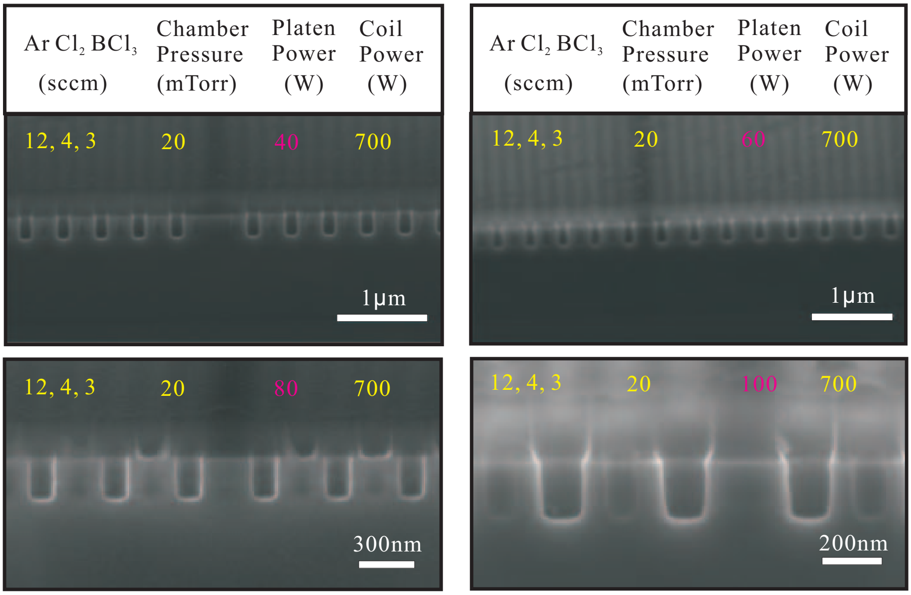
Ar Cl2 BCl3 (sccm)
Chamber Pressure (mTorr)
Platen Power (W)
Coil Power (W)
Ar Cl2 BCl3 (sccm)
Chamber Pressure (mTorr)
Platen Power (W)
Coil Power (W)
12, 4, 3
20
40
700
1μm
12, 4, 3
20
60
700
1μm
12, 4, 3
20
80
700
300nm
12, 4, 3
20
100
700
200nm

Figure 2.7: SEM image of the holes etched by recipes with different platen powers. The platen power is varied from 40 W to 100 W

and look a little bit tapered for the high platen power (100 W). This reflects a transition of the dry etch from a chemical reaction dominated to a physical sputtering dominated process. Fig. 2.8 shows the SEM images with different coil powers spanning from 300 W to 1000 W. Clear undercuts of the holes are observed in the samples made by low coil powers because the ions generated by coil are so few that very few ions can accelerate and sputter to the surface of the sample. We have also examined the robustness of our recipe by varying the gas flow of Cl_2 and BCl_3 in a small range and we get stable and good etch results.

The final dry etch results after systematical optimizations are shown in Fig. 2.9(a). The holes in Fig. 2.7 show both excellent uniformity and verticality of the sidewall. The holes reach deeply into the AlGaAs layer while 160 nm e-beam resist still remains after the dry etch, showing both high etch rate and selectivity. Fig. 2.9(b) clearly shows the high quality of the hole after removing the e-beam resist. We notice that the holes are uniform, presenting vertical sidewalls. Besides, the holes etched in AlGaAs layer exhibit the same

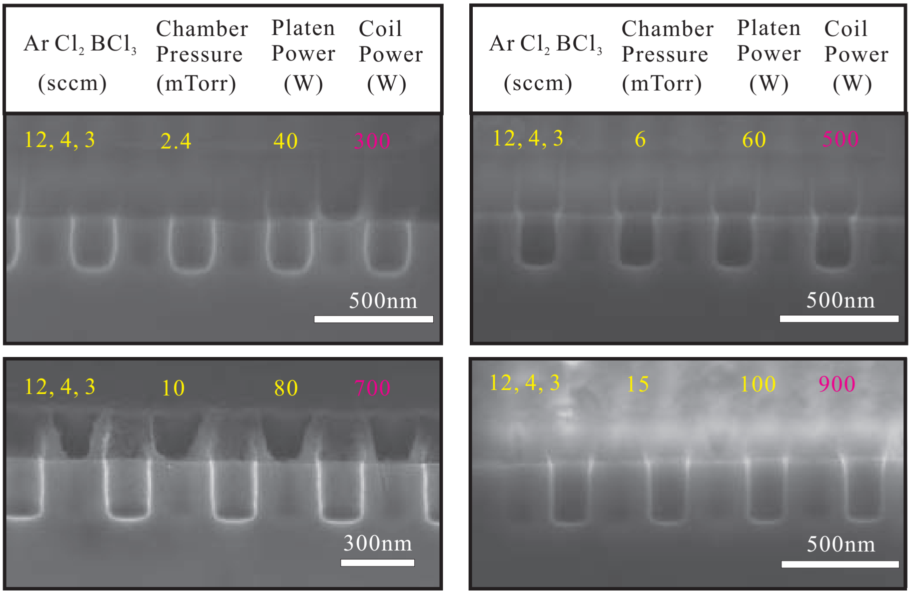
Ar Cl$_2$ BCl$_3$ (sccm)
Chamber Pressure (mTorr)
Platen Power (W)
Coil Power (W)
12, 4, 3
2.4
40
300
500nm
Ar Cl$_2$ BCl$_3$ (sccm)
Chamber Pressure (mTorr)
Platen Power (W)
Coil Power (W)
12, 4, 3
6
60
500
500nm
12, 4, 3
10
80
700
300nm
12, 4, 3
15
100
900
500nm

Figure 2.8: SEM image of the holes etched by recipes with different coil powers. The coil power is varied from 300 W to 900 W

uniformity and verticality as the holes in GaAs layer, which indicates that our recipe is general and can be applied to fabricate AlGaAs PC structures.

We sum up this section by identifying the roles of the each ICP parameter in our dry etch process. Some of our conclusions are general and can be used as a guide for redeveloping the same process in a different machine. First of all, an appropriate gas composition is highly desirable since it determines the reactive radicals and ions in the dry etch. In our process, chlorine is the main chemical etchant in the process. Empirically, better smoothness and anisotropic profile are observed in the BCl_3-based etching. Ar is a heavy element and provides the physical part of the dry etch. Once the gas composition is fixed, proper gas flow rates should be developed. The ratio of gas flow for different gases used in the etch largely determines the composition of the ICP generated plasma which could be dominated by physical ion component or chemical reactive species (neutrals and ions). Proper flow rates for different flow gases are highly required for our dry etch to obtain a plasma with balanced physical and chemical component. Chamber pressure significantly changes the etch rate

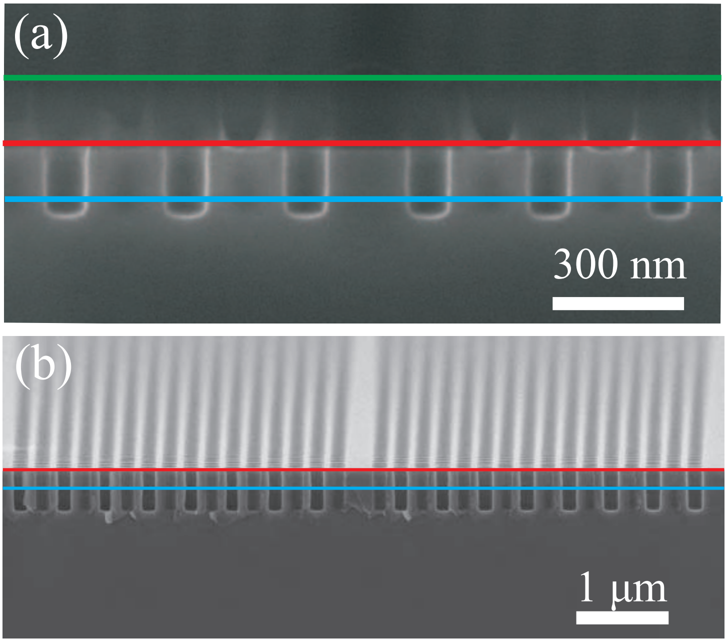

Figure 2.9: Final dry etch results after extensive optimizations. (a) SEM image of the etched holes with e-beam resist on top. (b) SEM image of the etched holes after removing e-beam resist. Green line:interface between the e-beam resist and air. Red line:interface between e-beam resist and GaAs layer. Blue line:interface between GaAs and AlGaAs layer.

and selectivity in our process and it should stay high to realize a high etch rate and high selectivity. The platen power gives rise to an acceleration voltage for the ions used for physical bombarding to the surface of the sample. By varying this parameter, the physical part in the dry etch can be manipulated. A platen power between 70 W- 80 W is best for our dry etch. Coil power Controls the density of the dissociated plasma consisting of ions and reactive radicals.

2.1.4 Release of the free-standing membrane structures

Releasing the free-standing membrane structures is a highly selective wet etch process. $\mathrm{Al_xGa_{1-x}As}$ can be removed by hydrofluoric acid (HF) for Al fractions $x > 0.5$ while GaAs almost does not etch in HF[16]. We remove the ZEP resist in a resist remover (Microposit Remover 1165) heated to 60 °C. An ultrasonic with the lowest power is applied to facilitate the removal of the resist. The complete removal of ZEP resist has been carefully examined by both an optical microscope and a SEM in Fig. 2.10. The surface of the wafer looks smooth and uniform in Fig. 2.10(a), which indicates that the resist has been fully removed from the surface. This conclusion has been further confirmed by a SEM image of the cross section of the sample in Fig. 2.10(b). Since the holes reach the AlGaAs layer, the HF solution can flow into the PC holes, and selectively etch the 1 μm sacrificial AlGaAs layer.

We use liquid HF acid solutions with different concentrations to release the membrane structures made in a 'passive' wafer and the results are shown in Fig. 2.11(a),(b). The etch rate can be estimated by investigating the undercut of a test sample under an optical microscope. All of the samples after the HF etch show an undercut in AlGaAs layer while the GaAs layer remains intact during the HF etch process. However, the undercuts are not complete and significant residues have been generally observed under the membrane structures. The amount of the residues increases with the reduction of the concentration of the HF acid, which is unexpected as generally low concentration of reactants favor reaction-controlled etching. The undercut obtained by a high concentration HF shows different etch rates for different crystal planes, which is a feature of reaction-limited wet etch process. We have tried to remove these residues by using chemical and physical methods but unfortunately we find it is impossible, to our best knowledge, to remove them as soon as they formed in the HF etch. We later figure out that this problem links to the 'passive' wafers grown by MOCVD (Purchased from LandMark Optoelectronics Corp in Taiwan).

A wafer with QDs embedded grown by MBE has been used for undercut tests by liquid HF with different concentrations, shown in Fig. 2.11(c),(d). The trend of the undercut with increasing concentrations of HF is consistent with what has been observed in the 'passive' wafer grown by MOCVD. In a low concentration HF etch, we find very strange shaped undercut residues, i.e., nanowires form under the membrane and penetrate via the etched holes to the surface of the membranes. These residues totally disappeared in a high concentration HF etch, which is different from the fact that a few residues left in a 'passive' wafer.

Inspired by a technique called vapor phase etch widely used in micro-

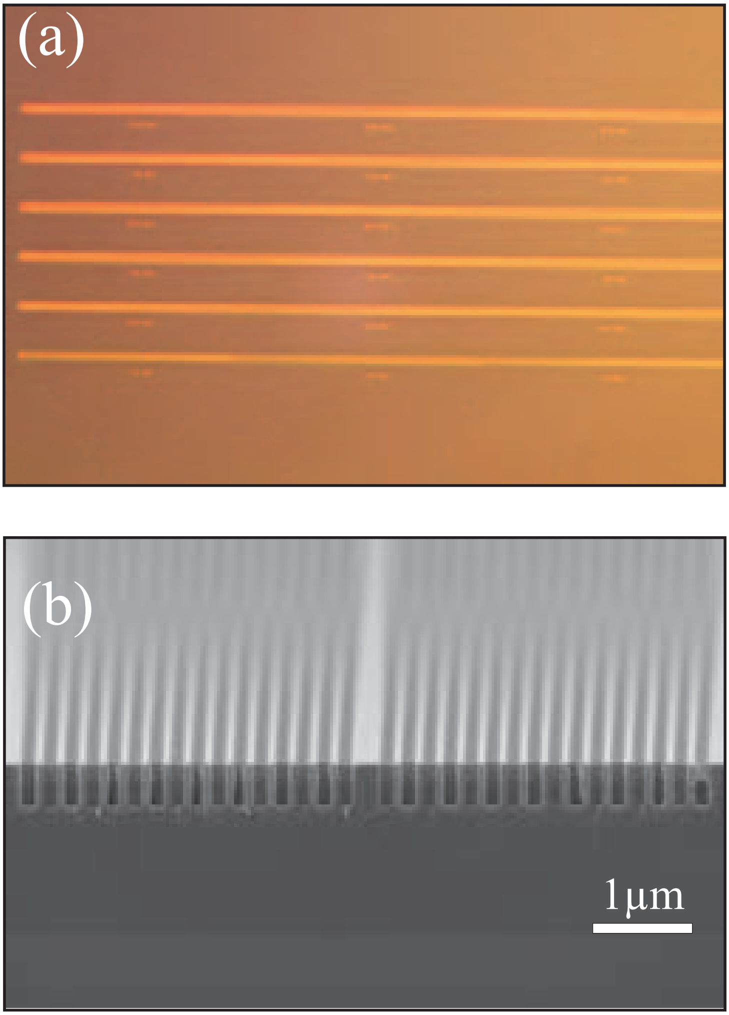

Figure 2.10: Removal of the e-beam resist. (a) Microscope image of the wafer surface after removing the e-beam resist. (b) SEM image of the cross section of the sample after removing the e-beam resist.

electromechanical systems (MEMS)[17], we adopt the vapor phase etch concept into the undercut process for the ’passive’ wafer. Fig. 2.12 shows the sketch of experimental scheme for a standard HF wet etch and our HF vapor phase etch. In the standard HF wet etch process, the wafer is directly dipped into the HF

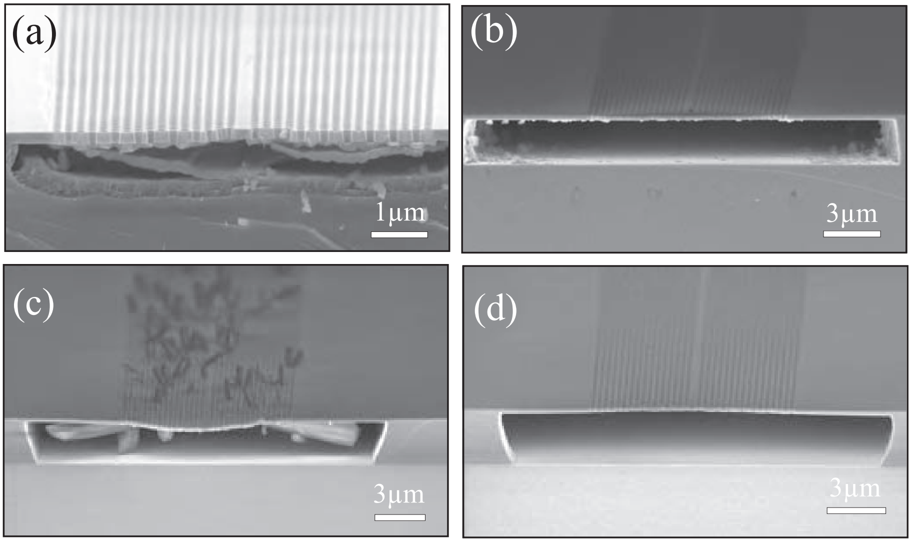

Figure 2.11: Underetch of 'passive' (a),(b) and 'active' (c),(d) wafers by HF with different concentrations. (a),(c) 5% HF. (b),(d) 40% HF.

solution while during the vapor phase etch process the wafer is exposed to the HF gas evaporated from HF liquid and confined into a closed space.

The undercut formed by using a vapor phase etch is shown in Fig. 2.13, where a clean undercut without any residue has been observed. The sharp and angular undercut surface indicates different etch rates for different crystallographic planes, which is a signature of a reaction-controlled process. The exact physical mechanism of such a nice undercut by vapor phase etch is not very clear because it specificly relates to the 'passive' wafers but may be due to the fact that these wafers are grown by MOCVD. One possible explanation for it is that the HF diffusion process in vapor phase condition is more efficient than that in a standard wet etch process, which gives rise to a reaction-limited etch process.

Although the vapor phase etch can lead to a nearly perfect undercut without any residues we find part of our membrane structures collapse during the undercut process, shown in Fig. 2.14(a),(b). The microscope image of the test structures clearly shows damage of the membranes structures and this is further confirmed by the SEM image where a few breakdowns denoted by the red

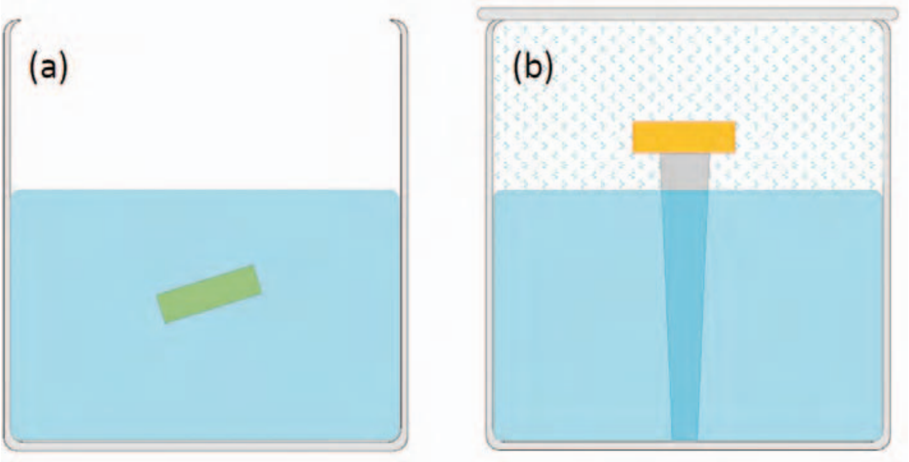

Figure 2.12: Schematics of the standard wet etch and vapor pase etch. (a) Standard wet etch. (b) Vapor phase etch.

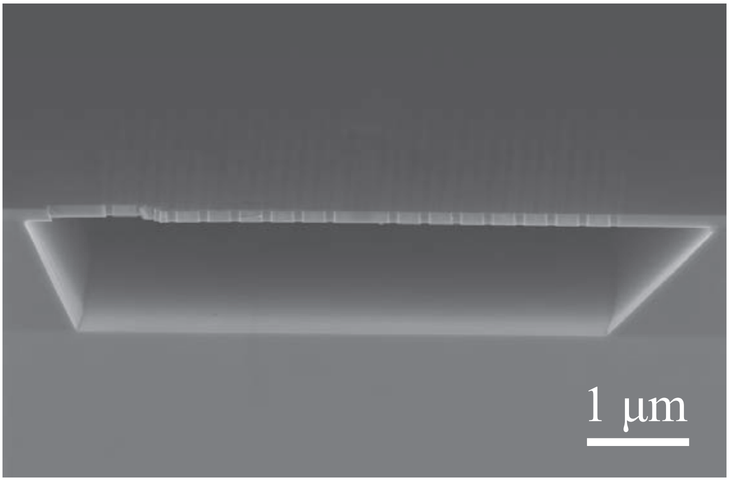

Figure 2.13: SEM image of cross section of the wafer after a vapor phase etch.

arrows in a membrane are shown. In order to maintain the mechanical stability of the membrane structure, a reduced etch rate for vapor phase etch is highly needed and it is realized by placing the beaker with HF inside on a cold plate. Another beaker with water inside has been used as a temperature reference

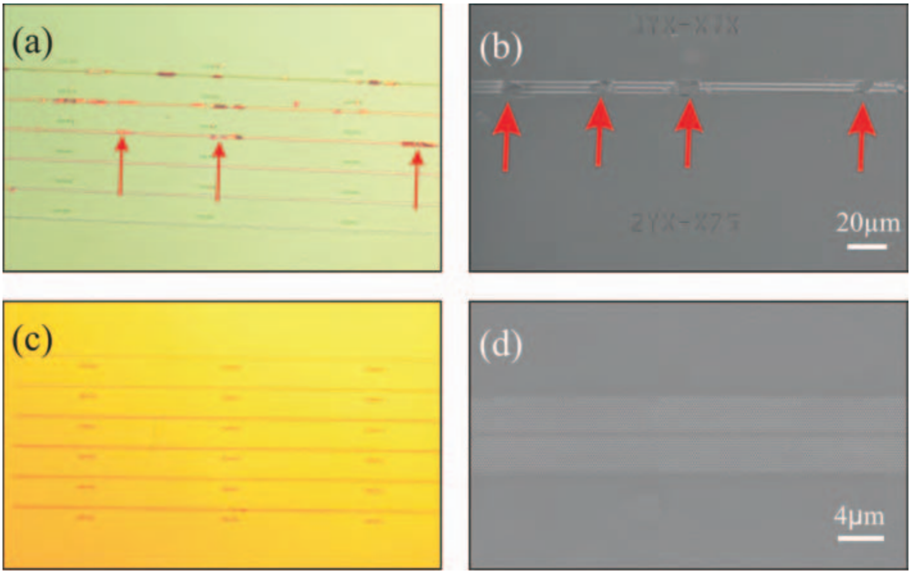

Figure 2.14: Comparison between room temperature and low temperature vapor phase etch. (a) Microscope image of a wafer after a room temperature vapor phase etch. (b) SEM image of photonic crystal structures after a room temperature vapor phse etch. (c) Microscope image of a wafer after a low temperature vapor phase etch. (d) SEM image of photonic crystal structures after a low temperature vapor phase etch. The red arrows indicate breakdowns of the membrane.

from which the temperature of the liquid on the cold plate is measured. By using vapor phase etch at 6 °C, suspended membrane structures without any damages are obtained and presented in Fig. 2.14(c),(d).

A undercut region can be clearly identified from a SEM image of a full undercut device, as shown in Fig. 2.15(a). In Fig. 2.15(b), a cross section of the device is presented. We have achieved smooth, straight sidewalls through a 160 nm GaAs membrane with a very clean undercut.

2.1.5 Post-cleaning of the sample

A close inspection into the surface of a final device reveals that sometimes that there are micro-sized residues left after the release of the membrane, which

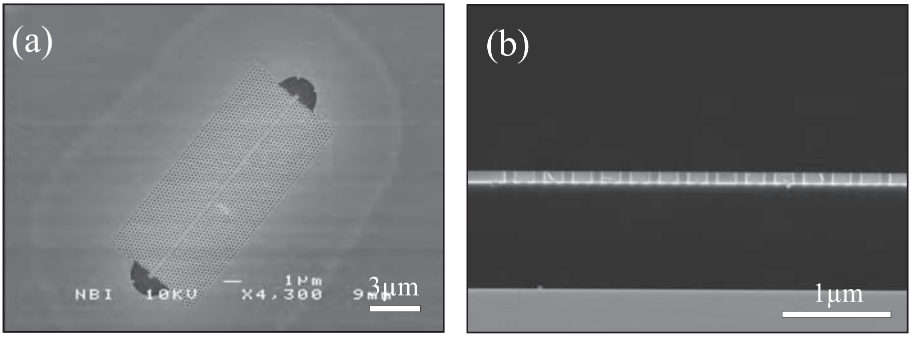

Figure 2.15: SEM images of the final devices. (a) SEM image of the surface of the final device. (b) SEM image of the cross section of the final device.

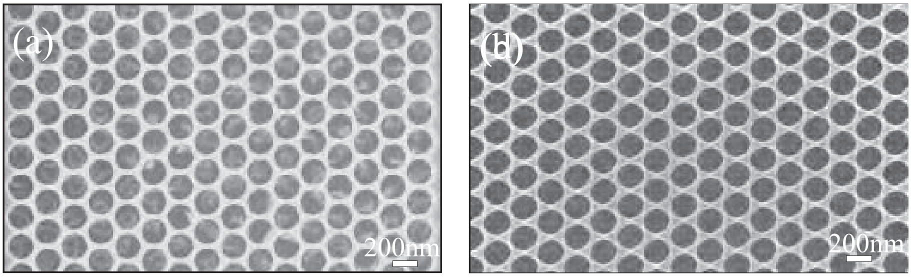

Figure 2.16: Comparison between the samples with and without cleaning processes. (a) SEM image of the PCs membrane before cleaning processes. (b) SEM image of the PCs membrane after cleaning processes.

serves as a main scattering source for the light, shown in Fig. 2.16(a). These residues sit both under and above the membrane structures, which could come from the resist and AlGaAs layer. The remnant resist can only be removed by oxygen plasma while the submicron-sized particles speculated to be hydroxide of aluminium can be removed in potassium hydroxide (KOH) solutions. The fabricated PC membranes have been post-cleaned with oxygen plasma and KOH (25 g/100 ml deionized water) solution[18]. The surfaces of the devices after the cleaning process are shown in Fig. 2.16(b). All residue under and above the membranes are effectively removed, which gives rise to a possibility to achieve a strong light-confinement for quantum electrodynamics experiments.

2.2 High-Q GaAs optomechanical nanomembranes

2.2.1 Introduction

The mechanical effect of light is an important aspect of light-matter interaction and one of the most famous examples is the comet tail pointing away for the sun. Today, optical force is widely used to precisely control the position of micro to nano-particles, referred to as optical trapping or optical tweezers[19]. Radiation pressure has been used as a tool for the detection of gravitational wave[20] for a long time. With the advance of modern nanofabrication technologies, the mechanical effects on micro-resonator have been extensively investigated[21, 22]. Cooling and amplification of mechanical motions of micro-resonators have been realized by utilizing a 'dynamic back action' effect due to the finite lifetime of photons in an optical cavities[8]. Ultimately the coupling between photons and mechanical motions should allow the observation of quantum mechanical behavior in micro- or nano-resonator[23, 24].

Incorporating direct band gap semiconductor materials in cavity optomechanics exhibits unexplored prospects due to a number of advantageous properties. In particular, GaAs enables the integration of optoelectronic functionality with nanomechanical elements[25]. The noncentrosymmetric nature of zinc-blende crystal structure of GaAs results in an appreciable piezoelectric coefficient, enabling efficient actuation or transduction[26]. Furthermore, there is a proposal of cooling down the lattice temperature of semiconductors down to 10 K, referred as optical refrigeration[27], although experimental demonstration has not yet been realized. QDs embedded in GaAs also enable strong coupling between a photon and a confined exciton[28]. Much effort has been invested in fabricating GaAs-based micro-resonator[29, 30] and improving their mechanical properties by strain engineering[31]. Coupling the intrinsic physical properties of direct band gap semiconductor to mechanical modes would enable a multitude of effects within cavity quantum optomechanics engineering[32]. Very recent results on both GaAs disk resonators[33, 34] and InP PC cavities[35] show the feasibility of realizing optomechanical systems in direct band gap semiconductors, but it is widely observed that GaAs micro-resonators suffer from low Q-factors, which limit the optomechanical cooling performance. In this section, we will present the experimental realization of millimeter-sized single-crystal GaAs nanomembranes with extremely high-Q-factor that have

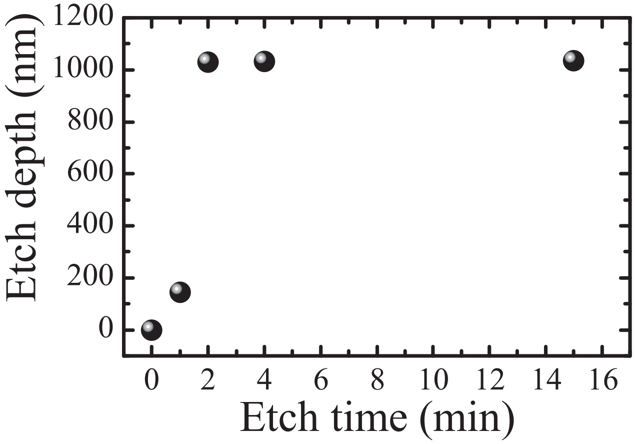

Figure 2.17: Etch depth of SiO_2 on the backside of the wafer as a function of etch time.

very promising applications.

2.2.2 Fabrication of High-Q GaAs optomechanical nanomembranes

The GaAs membrane is fabricated from a 'passive' wafer, which is shown in Fig. 2.1(b). The first step is to remove the substrate with citric acid/H2O2 solution (4 Citric acid (50% by wt.)/1 H2O2 (30%)) wet etch by using AlGaAs as an etch stop layer[36]. Then a non-buffered HF (10%) selective wet-etching follows in order to remove the AlGaAs sacrificial layer[16]. The single-crystal nanomembranes made by our method are optically accessible from both sides, which enables implementing cavity optomechanical cooling schemes.

The first and also very important step in our fabrication process is to remove the substrate of the wafer to make it optically accessible form both sides of the wafer. An appropriate mask should be used in a very long wet etch process. In the first round of the fabrication, we try to use a hard mask made of SiO_2 as we believe it will give rise to a higher selectivity than that given by a soft mask (photoresist). We deposite thin layers of SiO_2 with different thicknesses on both sides of the wafer by plasma-enhanced chemical vapor deposition (PECVD). The thicknesses of the SiO_2 layers on the front and back sides are respectively 350 nm and 150 nm. A photoresist (AZ 5214E) is spun on the backside of the wafer and a hole with a radius of 1 mm is defined by photolithography. The next step is to open a hole on SiO_2 hard mask by using HF wet etch. Since the SiO_2 layer on the front side of the wafer will be also etched by HF, we have to calibrate the etch time very carefully to ensure the opening on the backside can be achieved while the SiO_2 on the front side still remains after the HF etch. The etch depth as a function of etch time is shown in Fig. 2.17. We found a steady etch rate of HF on SiO_2 in the first two minutes however it seems to diverge after two minutes. Similar results are obtained by using buffered hydrogen fluoride (BHF) and diluted BHF, which indicates the inhomogenities of the deposited SiO_2 layer.

To reveal the reason behind such a highly nonuniform etch rate, the surfaces of the samples for different etch time are investigated with a microscope, which is shown in Fig. 2.18. Small pin holes on the surface of SiO_2 start to appear from the second minute and become more obvious with time, which indicates that the deposited layer is nonuniform. Pinholes in SiO_2 are known as a problem for a PECVD process. Based on this etch test, we find it is impossible to accurately control the etch rate of HF on SiO_2 deposited by PECVD.

In the second round of the fabrication, we use directly a thick photoresit on the backside as a single mask for etching through the GaAs substrate. The etch rate of the citric acid used in our process is estimated as 6 nm[13], which requires around 20 hours to etch through the substrate. We have examined two samples after etching for 20 hours in Fig. 2.19. For the first sample corresponding to Fig. 2.19(a),(b), the SiO_2 layer on the front of the wafer is broken down into small pieces of glass, indicating that the SiO_2 layer is not able to endure a long etch process. On the other sample, corresponding to Fig. 2.19(c),(d), the damage of the SiO_2 layer is so severe that the GaAs layer underneath is etched away in the citric etch process. We conclude that the deposited SiO_2 can not protect the GaAs layer in a long-time citric wet etch.

In the last round, photoresist (AZ 5214E) with a thickness of 3 μm is coated on both sides of the wafer and the patterns of the holes with different diameters ranging from 500 μm to 1 mm are defined by photolithography. After 30

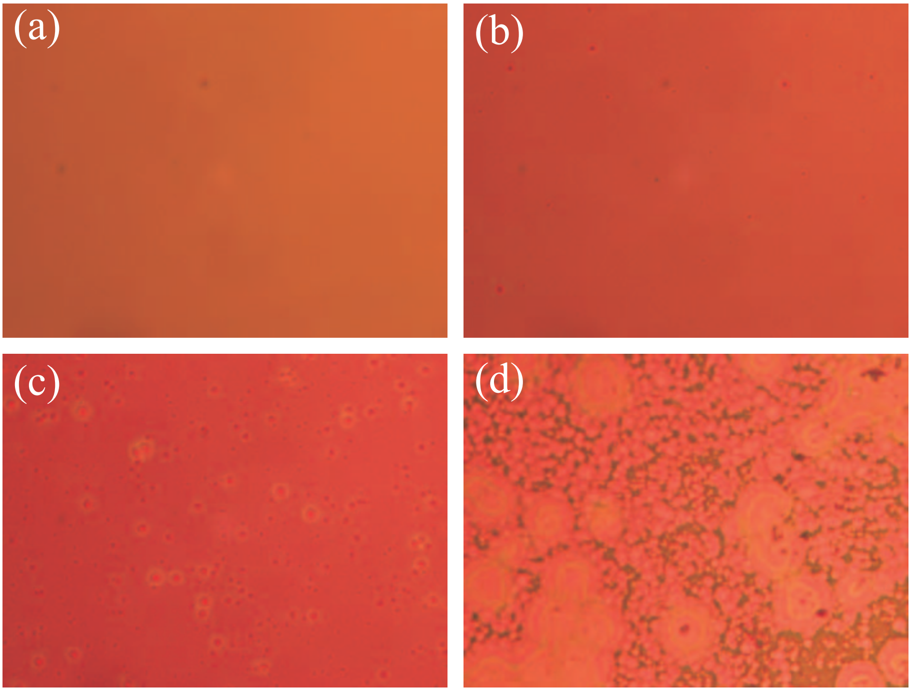

Figure 2.18: Microscope images of the SiO_2 layer for different etch time. (a) 1 min. (b) 2 min. (c) 2 min. (d) 4 min.

minutes hard baking at a temperature of 140 °C on a hotplate, the wafer is immersed into citric acid/H_2O_2 solution with magnetic stirring for 20 hours to etch through the GaAs substrate. Thanks to the excellent etch rate selectivity for GaAs versus AlGaAs in the citric acid/H_2O_2 solution, the 160 nm GaAs layer is intact due to the protection of the AlGaAs layer and the photoresist during the citric acid wet-etching as shown in Fig. 2.20.

Once the substrate is etched away, another selective wet-etching follows to remove the AlGaAs sacrificial layer and finally a GaAs nanomembrane is formed after removing the photoresist. Again, we have observed that often a thin layer of photoresist and submicron-sized particles are left after the completion of photoresist removal, which is shown by the scanning electron micrograph (SEM) in Fig. 2.21(b). These residues can be significant sources of light scattering and deteriorations of mechanical Q-factors. The same cleaning process as we applied

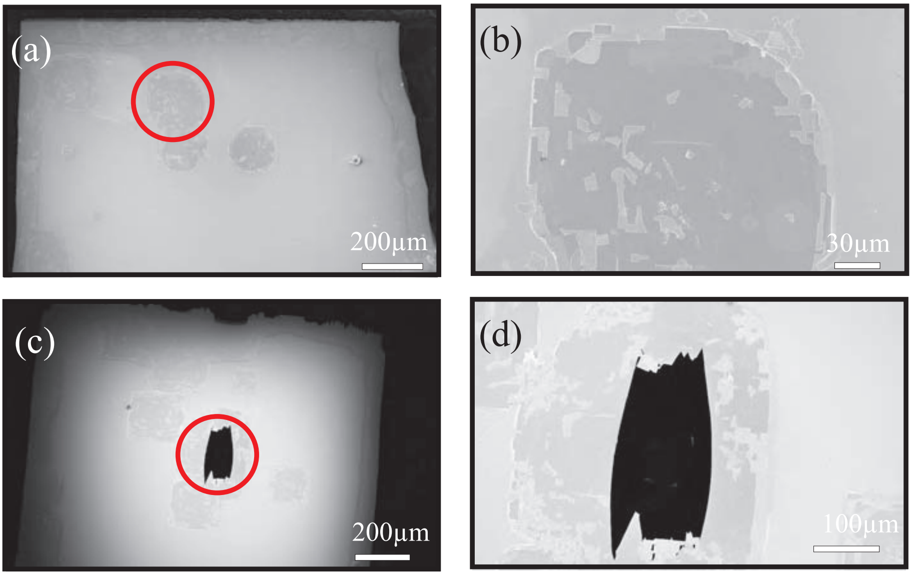

Figure 2.19: Damage of the SiO_2 layer on the front side of the wafer after citric acid etch. (a) SEM image of the front side of one wafer after citric acid etch. (b) Zoom in of the area marked by the red circle in (a). (c) SEM image of the front side of the other wafer after citric acid etch. (d) Zoom in of the area marked by the red circle in (c).

to the PC membranes is used to clean the GaAs nanomembranes. Fig. 2.21(c) shows SEM of a nanomembrane after the oxygen plasma and KOH cleaning processes. We find that the shapes of the fabricated nanomembranes deviated significantly from the circular photolithography masks. This comes from the different etch rates for different crystallographic planes of GaAs in citric acid. A close inspection of the membranes reveals that they are not completely flat, but rather they are bowing with an amplitude at the center of the membranes on the order of a few microns. The size of the largest nanomembrane made by our method is roughly 1.36 mm in width and 1.91 mm in length.

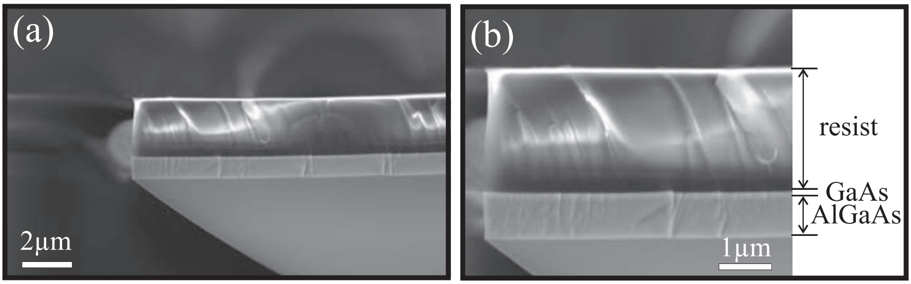
(a)
2μm
(b)
resist
GaAs
AlGaAs
1μm

Figure 2.20: (a)SEM image of the cross section of wafer after citric wet etch. (b) Zoom in of (a) in which the photoresist, GaAs and AlGaAs layer have been indicated.

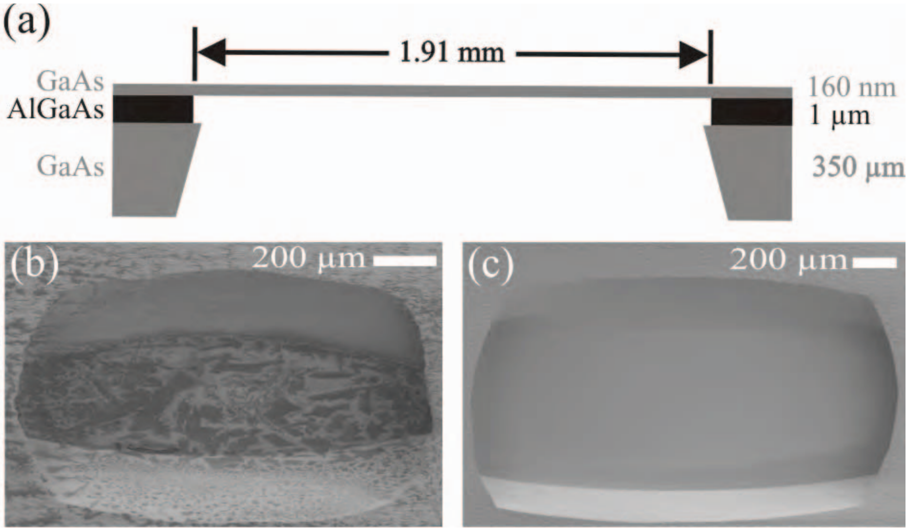
(a)
1.91 mm
GaAs
AlGaAs
GaAs
160 nm
1 μm
350 μm
(b)
200 μm
(c)
200 μm

Figure 2.21: (a) A cross section sketch of the nanomembrane. (b) SEM of the backside of the nanomembrane before and (c) after the cleaning process.

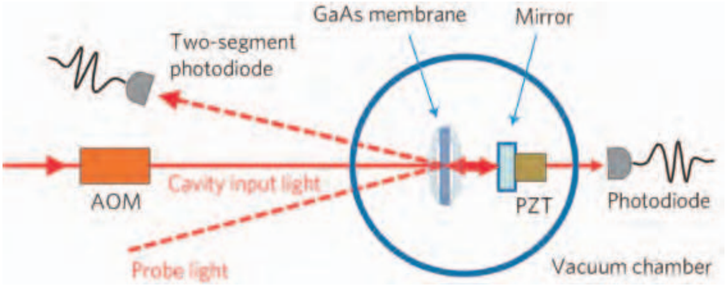

Figure 2.22: Sketch of the experimental setup. A dielectric concave mirror with the reflectivity of 96% and the membrane with the reflectivity of roughly 62% form a hemispherical cavity with the measured finesse of about 10 (essentially constant in the range of the laser wavelength from 810 nm to 884 nm). The cavity is placed in a vacuum chamber kept at 10^{-5} Pa. The cavity length ($\sim$ 29 mm) can be varied with a piezoelectric transducer (PZT) attached to the end mirror. A Ti:sapphire laser (810 nm - 880 nm) is used as a cavity input for both cooling and inducing mechanical oscillations (the beam spot size at the membrane is about 80 μm in radius) by modulating the intensity with an acousto-optic modulator (AOM). A diode laser (975 nm) is used to probe the membrane oscillations via a beam deflection method with a two-segment photodiode. *Figure by courtesy of Koji Usami.*

2.2.3 Characterizations of GaAs optomechanical nanomembranes

With the setup shown in Fig. 2.22[37], the Brownian motion of the membrane can be measured by either looking at the cavity field transmission or by using an external probe light via a beam deflection method. We have characterized the mechanical properties of the nanomembranes via frequency noise spectrum by using cavity transmission measurements. A dielectric concave mirror and a 160-nm-thick GaAs membrane form a cavity with the measured finesse of about 10.

By feeding the spectrum analyzer with the RF signal from the photodiode, we have observed 14 resonance frequencies ranging from 17.5 kHz to 59.5 kHz, see Fig. 2.23(a). The observed resonance frequencies conform within roughly 10% to the vibrational modes of a taut rectangular drumhead[38], where the resonance frequency for the (m,n)-mode is given by $\nu_{m,n} = \sqrt{\frac{T}{4\rho}((\frac{m}{L})^2 + (\frac{n}{W})^2)}$ with a membrane mass density $\rho = 5.36$ g/cm and a tensile stress T as a fitting parameter (the resultant T is 7 MPa), where L and W are the length and width of the membrane, respectively. The Q-factor is defined as $Q = \omega/\Gamma$ where $\nu = \omega/2\pi$ is the resonance frequency and Γ is the mechanical damping rate. Γ is measured through a ringdown measurement in which the ringdown of the mechanical modes is observed by inducing the oscillations with an intensity-modulated cavity field. A typical ringdown measurement for the (4,3)-mode is shown in the inset of Fig. 2.23(b). Due to the cooling effect the Q-factors and resonance frequencies vary with input powers in the ringdown measurements. The intrinsic mechanical Q-factors are extracted from the power-dependent ringdown measurements by extrapolating the Q-factors to zero cavity input power. Since the damping rate of a mechanical mode (i.e., inverse of Q) generally scales linearly with ν, $Q \times \nu$ is an important parameter for the mechanical characterizations. Table 1 lists the resonance frequencies, the corresponding Q-factors and the product of Q and ν for the modes we have carefully characterized. The highest Q-factor of 2.3×10^6 and $Q \times \nu$ value of 1.4×10^{11}, which is comparable to the state-of-the-art values for GaAs resonator[30, 33, 34], are found for the (4,3)-mode ($\nu = 59.5$kHz). We stress that much higher Q-factors for our GaAs nanomembranes are expected at cryogenic temperatures.

Table 2.1: Mechanical characteristics for the mechanical modes

Mode	Frequency (kHz)	Q-factor (10^6)	$Q \times \nu$ (10^{11})
(2,1)	23.4	0.50	0.12
(3,2)	45.5	0.56	0.25
(4,1)	47.5	0.53	0.25
(4,3)	59.5	2.3	1.4

The vibration amplitudes, which are proportional to the vibration speeds for a given resonance frequency, are mapped by a laser-Doppler vibrometer [MSA-500 Micro System Analyzer (Polytec Ltd)] with a white light interferometry method. Due to space limitations in the experimental method, these measurements were performed on a smaller sample (roughly 0.7 mm by 1.4 mm) than the one presented in Fig. 2.21. The vibration profiles of the

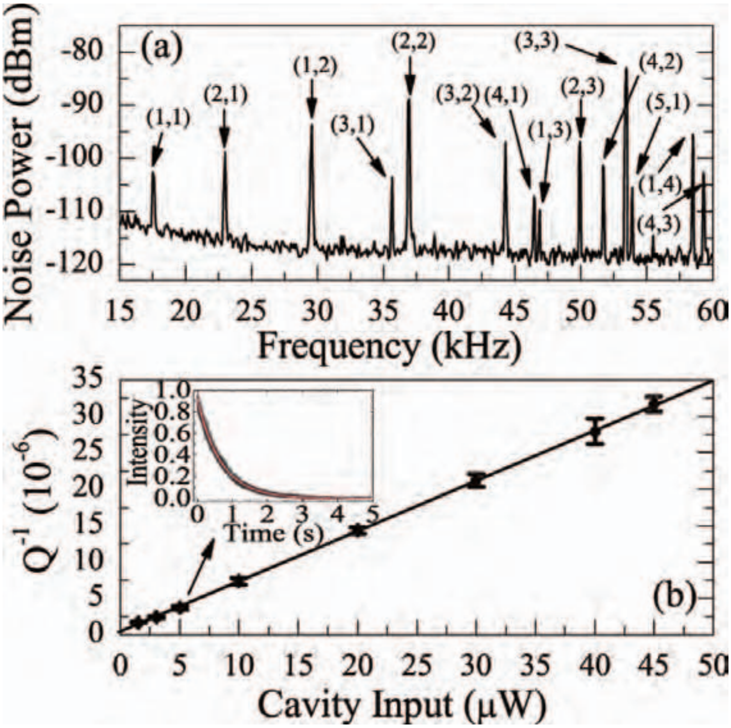

Figure 2.23: (a) Measured frequency noise spectrum in the 10 kHz - 60 kHz range presenting a series of peaks corresponding to the different mechanical modes labeled by the mode numbers in the parentheses. (b) Inverse Q-factor of the (4,3)-mode for different cavity input powers, the points are measurement data and the line is produced by a least-square linear fit. Inset: ringdown measurement with a cavity input power of 5 μW.

(1,1), (2,1), (1,3), and (2,2)-modes are shown on the left-hand side of Fig. 2.24 while the normalized vibration amplitudes of a taut rectangular drumhead ($a_{m,n}(x,y) = \sin(\frac{\pi m x}{L})\sin(\frac{\pi n y}{W})$ for the (m,n)-mode) are on the right-hand side. We find a good agreement between the measured mechanical mode profiles and the calculation. This model is also used to estimate the fundamental resonance frequency. The internal stress of the $\mathrm{Al}_x\mathrm{Ga}_{1-x}\mathrm{As}/\mathrm{GaAs}$ interface due to the lattice mismatch during growth can be approximated as[39] $133\times x$ and in our case $x = 0.85$. Thus, a tensile stress T of 110 MPa is predicted, which

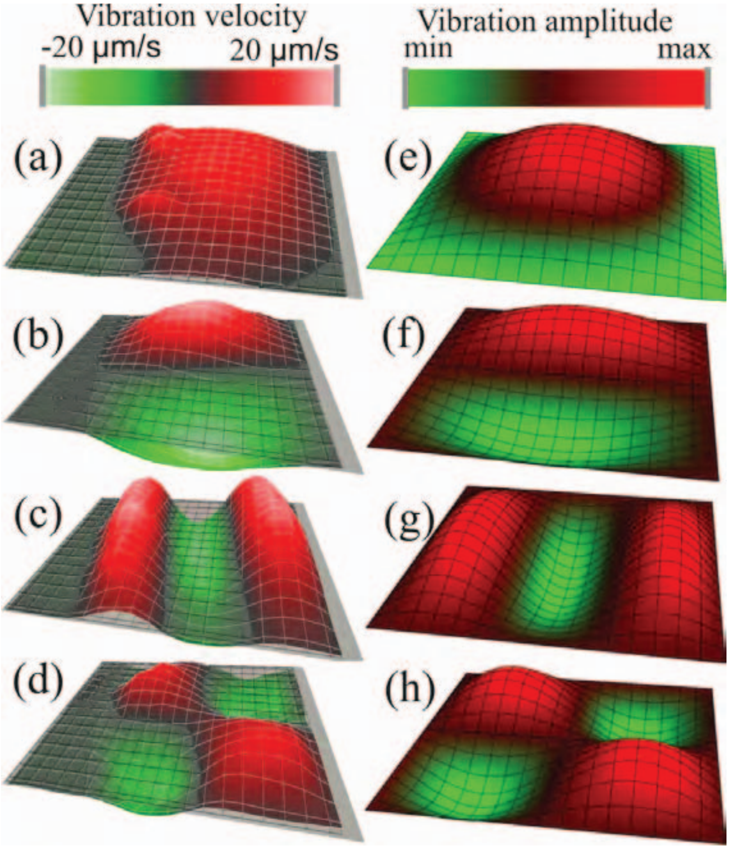

Figure 2.24: Analysis of the experimental and computed mechanical mode profiles. (a)-(d): Measured deformation profiles of the (1,1), (2,1), (1,3), and (2,2)-mode respectively with a micro system analyzer. (e)-(h): calculated mechanical mode profiles of the (1,1), (2,1), (1,3), and (2,2)-modes respectively according to a taut rectangular drumhead model.

leads to a fundamental resonance frequency (the (1,1)-mode) of 63 kHz. This is at variance with our findings (7 MPa and 23.4 kHz) and more investigations are needed to obtain a better understanding of the tensile stress development in the fabrication and the relation between the stress and high Q-factors in this system.

2.2.4 Applications of the GaAs optomechanical nanomembranes

In the cavity optomechanical cooling experiments performed on our High-Q GaAs nanomembranes, one of the mechanical modes has been cooled down from 300 K to 4 K and the cooling effect comes from the thermal relaxation of the carriers generated by the cooling laser with a energy higher than GaAs bandgap[37]. The cavity back-action cooling with the optically active semiconductors proved to exhibit very rich physics because of their internal electronic degrees of freedom, which may open up a new panorama for cavity optomechanics. Conversely, the intricate quantum process involving electrons, phonons, and photons in semiconductors could be explored by means of the strong optomechanical coupling.

2.3 Fabrication of wedged plasmonic waveguides

Plasmonic waveguides confine and guide light below the diffraction limit, which is crucial for further miniaturizing optoelectronic devices[40]. Due to the strong confinement of light in plasmonic waveguides, they can also be used as a powerful tool for enhancing light-matter interaction. Coupling single quantum emitters to plasmonic waveguides has been suggested as an efficient way for single-photon generation[41] and single-photon transistors[42].

Wet etch is usually isotropic, which leads to large bias when etching thick films. However, some wet etchants etch crystalline materials at very different rates depending upon which crystal face is exposed. This effect is highly desirable to achieve specific geometry in a single-crystal material with very smooth surfaces. For instance, potassium hydroxide (KOH) displays an etch rate selectivity 400 times higher in $< 100 >$ crystal directions than in $< 111 >$ directions. The wedged plasmoinc waveguides have triangular shaped cross section, which could be achieved if a proper etchant is chosen. We use electron beam lithography to define nanowaveguides with different orientations respect to the $< 111 >$ direction and try many chemical combinations for the wet etch. Finally, we obtain a sharp groove in to the GaAs substrate by using a solution mixed with sulfuric acid, hydrogen peroxide and de-ionized water. Metal evaporated onto such grooves inherits the smoothness at the interface between substrate and metal. This fabrication method results in smooth grooves etched into GaAs, as shown in Fig. 2.25(a).

In Fig. 2.25, the performance of a plasmonic waveguide has been examined by a finite-element method in which the Purcell enhancement for an in-plane dipole coupling to the fundamental plasmonic mode is calculated. Based on this calculation, a high Purcell effect can be achieved when the quantum dots are close enough to the metallic tip. However, bring the quantum dots to the vicinity of semiconductor-air interface gives rise to significant non-radiative recombinations. Although we have developed a technique to realize plasmonic structures with good smoothness inherent from the semiconductor surface formed by wet etch, more numerical simulations are needed to design structures which are able to work on quantum dots relatively far from the semiconductor-air interface.

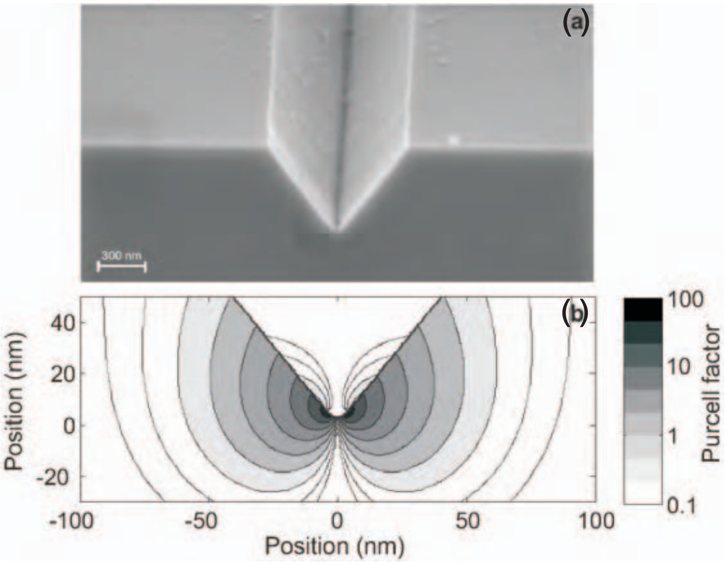

Figure 2.25: Coupling to a plasmonic wedge waveguide. (a) SEM picture of a wedged plasmonic waveguide before metal evaporation. (b) Purcell enhancement calculations for a dipole emitter coupled to the plasmonic wedge waveguide. The dipole is oriented horizontally and the metallic wedge which is surrounded by GaAs. *The Purcell enhancement calculation is performed by Yuntian Chen.*

2.4 Conclusion and outlook

We have developed various fabrication procedures for high-quality photonic and phononic nanostructures. For the PC membranes, a fabrication process directly based on an e-beam resit ZEP 520A has been developed and the fabricated structures exhibit smooth surface and highly vertical sidewalls. We expect that many novel cavity quantum electrodynamics phenomena such as Purcell effect and even strong coupling can be observed in these samples. We have also achieved the state-of-the-art optomechanical resonator with a world record mechanical quality factor up to 1 million. The cooling of a mechanical mode has been realized in this optically-active semiconductor nanomembranes by creating excitons with an above-band pumping laser.

With the fabrication technology developed in this chapter, single functional devices based on the coupling between single QDs and PC nanostructures have been realized. However, this coupling heavily relies on the spatial overlap between QDs and the anti-node of the cavity mode, which is highly unlike to achieve due to the random locations of the self-assembled QDs. Achieving deterministic coupling between QDs and PC devices is the next step to build the network for quantum information processing. Recently, significant breakthroughs have been shown by either using AFM[28] or in-situ lithography[43] techniques to obtain strong couplings with very high yields. One more step beyond this is the independent tuning of the QDs and cavities in different nodes of the quantum network.

For the optomechanical nanomembranes, incorporating semiconductor QDs in nanomembranes to cool the nanomechanical modes to its ground state[44] and patterning the nanomembranes for controlling of the coupling between phonons and photons can be envisioned in the future[45].

Chapter 3

Highly efficient single-photon emission and lasing in photonic crystal nanocavities

In this chapter, we perform both theoretical and experimental investigations on semiconductor QDs in PC cavities. In order to capture basic physics of light-matter interaction in our system, a simple but straightforward quantum optics model, Jaynes-Cummings model (JCM)[46], is employed in which the QDs are approximated as two-level atoms interacting with a single optical mode of PC nanocavities. Based on this model, we have identified prerequisites of single artificial atom lasers with realistic parameters measured in the experiments. In the experiments, two types of semiconductor quantum light sources, single-photon sources and nanolasers have been studied. The single-photon source based on QDs in PC nanovavities exhibits a high brightness which is quite remarkable due to the fact that light is confined in the high refractive index material where the QDs sit. A very smooth phase transition from spontaneous emission to stimulated emission has been observed with the increasing excitation powers, which is the signature of a nanolaser with a high spontaneous emission factor usually denoted as β. We further compare the experimental results of nanolasers to a more advanced semiconductor micro-cavity laser theory and a good agreement is obtained. We conclude that multi-exciton states generated under strong excitation powers play a very important role in the lasing process.

3.1 Introduction

3.1.1 Semiconductor quantum dots

Semiconductor QDs known as artificial atoms are the core elements in modern solid-state quantum photonics due to their superior electronic and optical properties. Among various types of QDs, self-assembled semiconductor InAs QDs grown by Stranski-Krastanov (SK) mode are extensively investigated and widely used for optoelectronic devices, as sketched in Fig. 3.1(a). In a self-assembly growth process, a very clean GaAs substrate is sitting in an ultra-high vacuum MBE chamber connected to different sources. GaAs mono-layers are firstly deposited. By depositing InAs molecules on top of GaAs layers, small island, referred as to QDs, are formed above a certain thickness due to the lattice mismatch between the GaAs and InAs. Finally a cap layer of GaAs is deposited to isolate the QDs from the environment. The random spatial distribution of QDs can be clearly seen with an atomic force microscope (AFM) before capping layer is deposited in Fig. 3.1(b). A distribution of the size gives rise to an inhomogeneous broadened emission when taking an optical spectrum of an ensemble of QDs. Although the site-controlled QDs have been developed, their quantum efficiency is yet not comparable to the QDs grown by SK mode. The electrons and holes are spatially confined in InAs QDs due to potential well exerted by the wider band gap of GaAs, which gives rise to a discrete energy for both electrons and holes sketched in Fig. 3.1(c). When shining a laser with energy higher than the band gap of GaAs, electrons and holes are generated in the conduction band and valence band respectively. By interacting with phonons, the excited electron hole pairs subsequently relax to the lowest state and finally emit a single photon by a radiative recombination process.

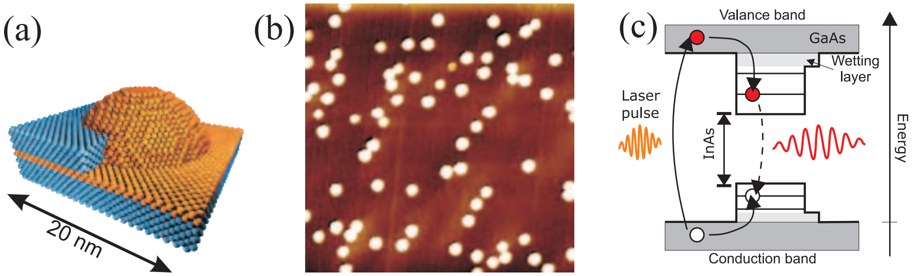

Figure 3.1: (a) Sketch of InAs QDs in GaAs matrix, the InAs QDs (yellow) are surrounded by GaAs Matrix. (b) AFM image of InAs QDs before the capping layer is deposited, the physical size in the image is 1 μm × 1 μm. (c) The discrete energy levels of QDs. Electrons and holes exited by a laser pulse relax into the lowest excited state and emit a single photon via radiative recombination.

3.1.2 photonic crystal cavities

As we have discussed in chapter 2 PC membrane structures can confine the light in three dimensions by employing the photonic band gap in-plane and total internal reflection in the vertical direction. Optical cavities can be created in PC membrane structures by locally introducing defects to perturb the periodicity. The cavities studied in this chapter are created by removing three consecutive holes to form a cavity in a PC membrane, firstly proposed as L3 type cavity by Noda's group[47]. This type of cavity exhibits high-Q-factors up to half a million while supports extremely low mode volumes down to cubic wavelengths, which is an ideal candidate of enhancing light-matter interactions. In the experiments the resonance frequency of the cavity can be engineered by designing different lattice constants and a fine tuning of the cavity resonance can be achieved by depositing inert gas on the surface of PC structures.

Fig. 3.2(a) shows a SEM image of a typical L3 cavity and the field profile of the fundamental cavity mode. By following the cavity design method: 'the light has to be confined gently in order to confine it tightly'[47], the three most inner holes next to the cavity area have been shifted by 17.5%, 2.5% and 17.5% of the lattice constant a from their original positions. The electromagnetic field is strongly confined in the area where three holes are missing. Standard L3 cavities have 6 optical modes with different polarizations. These modes can be

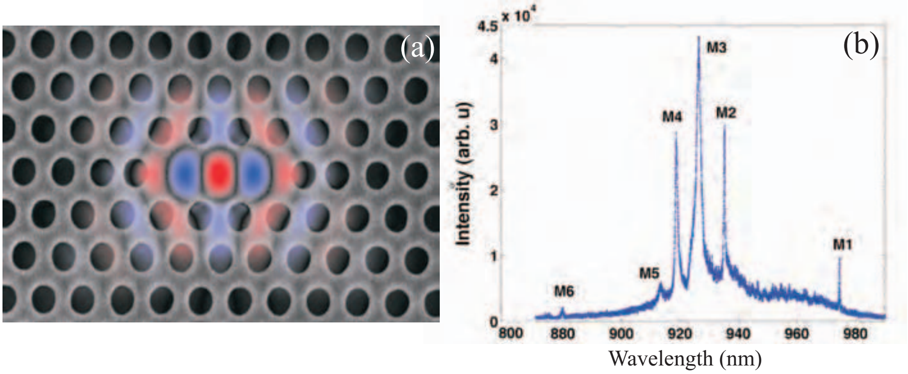

Figure 3.2: Characterizations of a typical L3 typep cavity. (a) SEM image of an L3 type PC nanocavity with a calculated mode profile of M1 on top. (b)Wide range spectrum of an L3 type nanocavity, showing 6 cavity modes denoted from M1 to M6.

probed by using QDs as internal light source to excite all of them. Fig. 3.2(b) shows a high power μ-PL spectrum of a L3 cavity. This spectrum has been taken in a certain output polarization in order to see all the cavity modes named from M1-M6. In our samples, M1, M2, and M4 modes have high-Q-factors in the range from 3000 to 8000, which is high enough to observe cavity-QED effects on a single QD level. Based on the output polarization dependent μ-PL measurements, M1, M2, M4, and M6 modes have the same polarization dependence while modes M3 and M5 show the opposite polarization. We note that the emission intensity of M3 is higher than all other modes and this behavior of a bright M3 mode has been observed in all L3 cavity structures with different lattice constants.

A main quantity of optical cavities is the quality factor, Q. The quality factor of a resonator is the ratio of the energy stored to the energy dissipated, and can be found from the center frequency ω divided by the spectral width of the line shape $\triangle\omega$, $Q = \frac{\omega}{\triangle\omega}$.

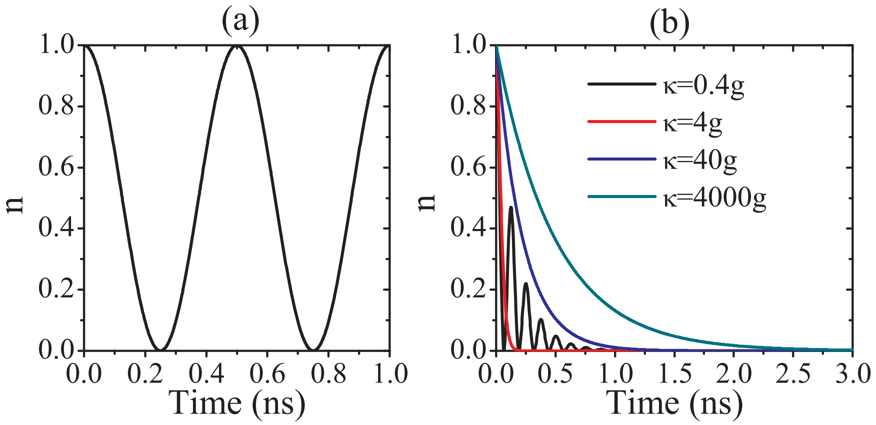

Figure 3.3: Time evolution of the population of a QD without dissipations (a) and with different cavity decay rates κ (b). The emitter is initially in the excited state. The coupling strength g=1 GHz in (a), $g = 25$ ns^{-1}, γ=1 ns^{-1} in (b).

3.2 Modeling single quantum dots in photonic crystal cavities

3.2.1 Jaynes-Cummings model

An full quantum mechanical model is highly desirable in order to describe the interaction between a single quantum emitter and a single cavity mode. The single quantum emitters can be approximated as two-level emitters. Since we only consider the interaction between the fundamental mode of the cavity and the spacing between the cavity modes is much larger than that between the QDs emission wavelength and the fundamental mode, the cavity mode can be approximated as a single-mode electromagnetic field. So a QD-PC cavity system can be described by the Jaynes-Cummings Model (JCM) in which a two-level atom with a frequency of ω_x is coupled to a single mode cavity with a frequency of ω_a, with a strength g. The detailed derivation of JCM can be found in a classic quantum optics book[48] and the full quantum evolution of this system can be described by the master equation

$$\dot{\rho} = -\frac{i}{\hbar}[\hat{H}, \rho] \tag{3.1}$$

where the total Hamiltonian of the system is ($\hbar = 1$ is used in the numerical calculations)

$$\hat{H} = \omega_x \hat{\sigma}^+ \hat{\sigma}^- + \omega_a \hat{a}^\dagger \hat{a} + g(\hat{\sigma}^+ \hat{a} + \hat{\sigma}^- \hat{a}^\dagger) \tag{3.2}$$

Here, $\hat{a}$ ($\hat{a}^\dagger$) is the annihilation (creation) operator for a photon in the cavity mode, while $\hat{\sigma}^-$ ($\hat{\sigma}^+$) is the lowering (raising) operator for the exciton. The detuning between the QD and the cavity is $\delta = \omega_x - \omega_a$. The dynamics of this system is obtained by numerically solving the master equation with the quantum optics toolbox developed by Tan[49]. Fig. 3.3(a) presents the time evolution of the population of a QD initially in the excited state. The basic coherent exchange of the populations between the QD and cavity mode with a frequency of $2g$ has been observed. This oscillation is referred to as vacuum Rabi oscillation. Here spontaneous emission process is reversible. A photon is emitted by the QDs and then stored in the cavity, this stored photon can be reabsorbed and reemitted again and again.

3.2.2 Jaynes-Cummings model with dissipations

Dissipation is an unavoidable process in any physical experiments. Introducing dissipation is critical to allow for any meaningful physical interpretations. Two dissipative processes have been neglected in ideal JCM. In reality, the two-level emitter decays to the ground state by coupling to the radiation modes and the electromagnetic field can leak out from an optical cavity due to the imperfections of the cavity mirrors. The dissipative processes can be handled in JCM by using a reservoir theory. The emitter decays to the ground state by coupling to a reservoir at a rate of γ and the electromagnetic field leaks to the reservoir at a rate of κ, as shown in Fig. 3.4. These processes can be described by Lindblad terms in the Schrodinger picture.

$$\dot{\rho} = -\frac{i}{\hbar}[H, \rho] + L[\rho] \tag{3.3}$$

where the Liouvillian $L[\rho]$ describes the nonhermitian evolution of the system which is caused by the coupling of the system to the reservoirs leading to irreversible dissipation. The Liouvillian must be of the Lindblad form[50] in order to preserve the trace of the density operator $Tr\rho = 1$:

$$L[\rho] = \sum_{i=1} \frac{\Gamma_i}{2}(2R_i\rho R_i^\dagger - \{R_i^\dagger R_i, \rho\}) \tag{3.4}$$

where Γ_i is the rate associated with the process given by the operator R_i. The operators associated with the QD and cavity decay rates are naturally chosen as the annihilation operators for the dot and field respectively. The damping part for both the dot and the cavity mode can be described by operators in the Lindblad form with the master equation, written as

$$\begin{aligned} L_{cav}[\rho] &= \frac{\kappa}{2}(2\hat{a}\rho\hat{a}^\dagger - \{\hat{a}^\dagger\hat{a}, \rho\}) \\ L_{at}[\rho] &= \frac{\gamma}{2}(2\hat{\sigma}\rho\hat{\sigma}^\dagger - \{\hat{\sigma}^\dagger\hat{\sigma}, \rho\}) \end{aligned} \tag{3.5}$$

By numerically solving Eq. 3.3 the decay curves for different values of the cavity decay rate κ can be calculated in resonance ($\delta = 0$) using typical values for QDs (g = 25 GHz, $\gamma = 1\,\mathrm{ns}^{-1}$). These decay curves are shown in Fig. 3.3(b). For the two lowest Q-factors corresponding to $\kappa = 4000g$ and $\kappa = 40g$ the decay is exponential and the decay rate is enhanced when the Q factor is increased. Once the system enters the strong coupling regime where $\kappa = 4g$, the decay is no longer exponential. In the strong coupling regime ($\kappa = 0.4g$) Rabi oscillation is observed. Here the population switches back and forth.

3.2.3 Modeling of a single artificial atom laser

In the previous section, we have included the dissipation processes of the QD and cavity in the JCM with Lindblad terms. This method is also valid for the reversal dissipation process such as optical pumping where carriers or photons can be injected from the reservoir to the system, as shown in Fig. 3.4.

To introduce a pumping mechanism on a QD, one has to add to the master equation a Lindblad operator

$$L_{pump}[\rho] = \frac{P}{2}(2\hat{\sigma}^+\rho\hat{\sigma}^- - \{\hat{\sigma}^-\hat{\sigma}^+, \rho\}) \tag{3.6}$$

Here P is the pumping rate. With the pumping term in our model, we are able to theoretically investigate the single QD lasers and this modeling can provide the information that the requirements of our experimental parameters for a

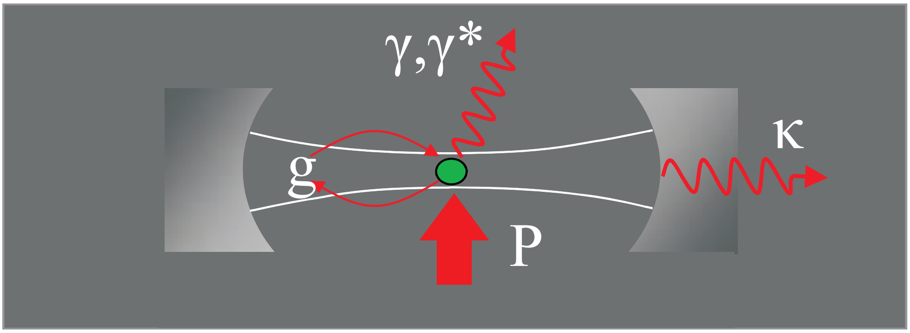

Figure 3.4: Schematic of a single QD and cavity mode system. The emitter decays to the ground state with a rate of γ and the photon leaks out of cavity with a rate of κ. The coupling strength between the atom and cavity mode is denoted as g, $\gamma*$ is the pure dephasing rate of the emitter. P is the pumping rate for the QD.

single QD laser. Here we are mainly concerned about whether the Q-factors of our PC cavities are high enough to meet the requirement of the single dot laser. If not, is the Q-factor needed for the single dot laser realistic to achieve by the current modern fabrication technology? We have studied the evolution of two main properties of the single emitter device with respect to the pumping rate, namely, the cavity population and the auto-correlation function of the field at zero time delay defined as $g_2(0) =< \hat{a}^\dagger\hat{a}^\dagger\hat{a}\hat{a} > /n_a^2$. In the numerical calculation, the value of the coupling strength g we used is 40 GHz reported in the literature[28], the spontaneous emission rate is 1 ns^{-1}. The single artificial atom laser is fundamentally different from the conventional lasers where the lasing threshold can be identified by the abrupt change of the output intensity at the lasing threshold. In the quantum laser theory for a single emitter, the cavity photons reaching unity is defined as the lasing threshold[51]. The onset of lasing can be also confirmed by the study of the statistics of the emitted field, that clearly shows a transition from anti-bunched ($g_2(0) < 1$) to Poissonian ($g_2(0) = 1$) distribution.

Fig. 3.5 presents the mean number of the cavity photons as a function of pumping rate for different cavity decay rates κ. In this model, the mean number of the cavity photon increases with the pumping rates. When the pumping rate is too large, the atomic emission becomes incoherent, leading to a decrease of

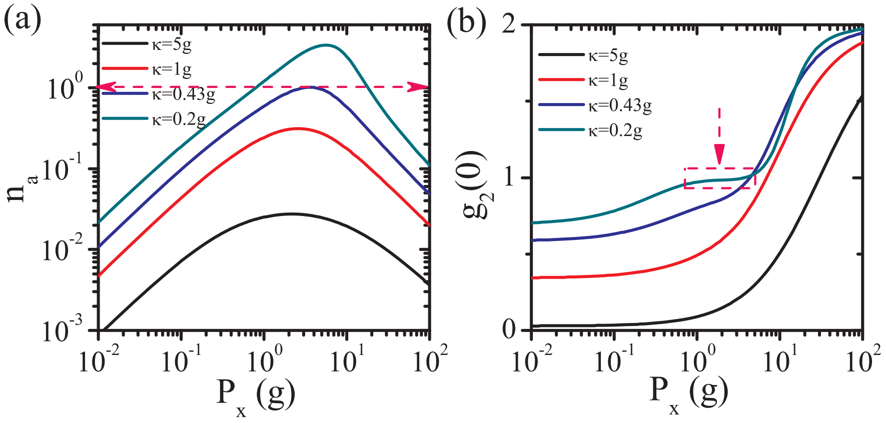

Figure 3.5: Numerically calculated (a) cavity population. (b) statistics of the emitted field as a function of pumping rate, for different cavity decay rates. The vertical line in (a) indicates the laser threshold. The clamping of $g_2(0) = 1$ highlighted by the arrow in (b) is an indication of stimulated emission.

the cavity population. The emitted field becomes thermal and the parameter $g_2(0)$ converges to 2. This phenomenon is known as quenching of the laser and was first predicted in ref [52]; it is attributed to the saturation of the two-level atom. The maximal number of the cavity photons increases with the decrease of κ. For $\kappa = 0.43g$, the lasing can be achieved with appropriate pumping rates. The laser threshold is shown by the vertical line in Fig. 3.5(a). The clamping of $g_2(0) = 1$ highlighted by the arrow in Fig. 3.5(b) is an indication of the realization of stimulated emission. The Q-factor corresponding to $\kappa = 0.43g$ ($g = 40$GHz) is 37,000 at 1 μm wavelength. The Q-factors of silicon PC cavities[12] are much higher than this number and the highest Q reported for GaAs PC cavities is 170,000[53], also much higher than this number. Although it is widely observed that introducing InAs QDs in GaAs PC cavities degrades the Q-factors, we believe that single QDs lasing with PC cavities is still feasible with current nanofabrication technology.

In a solid-state environment, the quantum emitters unavoidably interact with the lattice vibrations, which broadens the transition between to the discrete levels of QDs. This process can be generally described in the frame of pure dephasing. For a physical process mediated by an optical cavity, a spectral

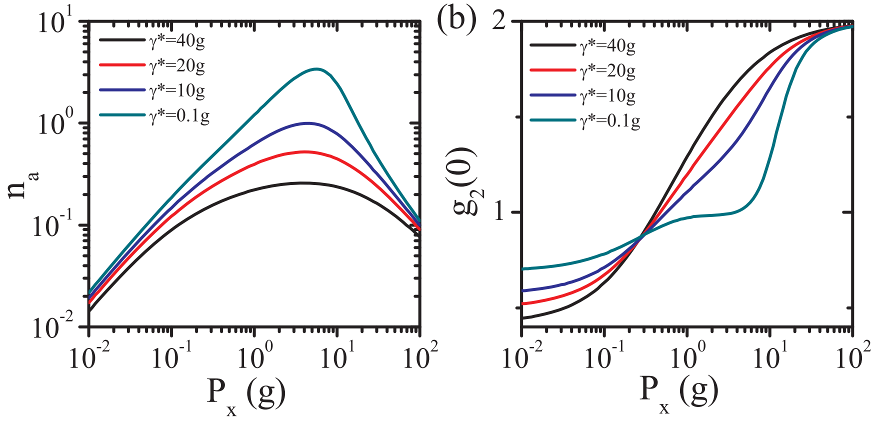

Figure 3.6: Numerically calculated (a) cavity pupolation. (b) statistics of the emitted field as a function of pumping rate, for different dephasing rates.

resonance between an emitter and a cavity mode is needed. Normally, fine tuning techniques of both an emitter and cavity is used when coupling an emitter to a cavity. Broadening the emission from an emitter by pure dephasing is an unexplore degree of freedom to engineer the light-matter coupling. The pure dephasing can be easily implemented in our model by adding a Lindblad term as follows:[54]

$$L_{deph}[\rho] = \frac{\gamma*}{2}(2\hat{\sigma_z}^{+}\rho\hat{\sigma_z}^{-} - \{\hat{\sigma_z}^{-}\hat{\sigma_z}^{+}, \rho\}) \tag{3.7}$$

where $\gamma*$ is the pure dephasing rate and $\hat{\sigma_z} = \frac{1}{2}[\hat{\sigma_+}, \hat{\sigma_-}]$. First we examine the effect of dephasing on the single dot lasing on the resonance condition ($\delta = 0$). As shown in Fig. 3.6, with the increasing pure dephasing rate, the mean number of photons gets reduced and the vanish of lasing can be clearly seen with a dephasing rate of $\gamma* = 20g$. We note that the clamping of the autocorrelation function to the Poissonian value $g_2(0) = 1$ disappears. The lasing is also lost when increasing the detuning as shown in Fig. 3.7. For a detuing of $\delta = 5g$, the signatures of lasing disappear totally both by in the mean photon number in the cavity and the $g_2(0)$. For a slightly small detuning of $\delta = 2g$, the mean number of photons in the cavity can still be larger than 1 but the clamping of $g_2(0) = 1$ gets worse, which indicates a degrade of lasing

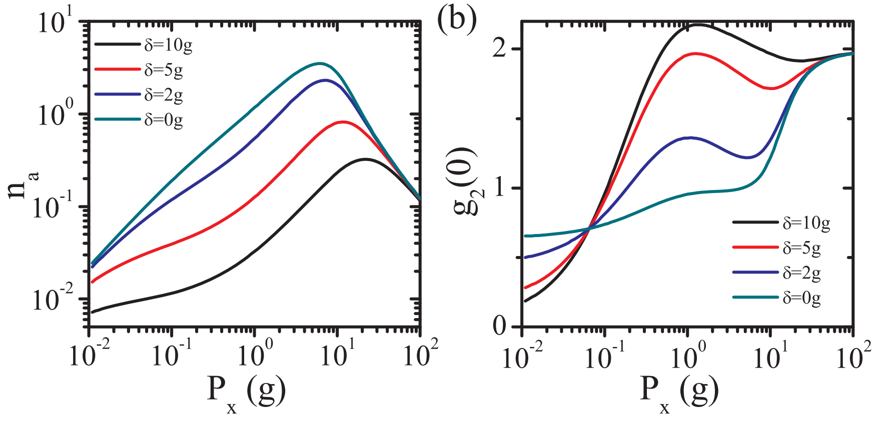

Figure 3.7: Numerically calculated (a) cavity population. (b) statistics of the emitted field as a function of pumping rate, for different detuning rates.

in the viewpoint of photon statistics. This degrade of lasing is compensated by introducing an appropriate dephasing rate shown in Fig. 3.8. Although the lasing can be achieved for dephasing rates of $\gamma* = 0g, 1g$ with a detuning of $\delta = 2g$ by looking at the mean number of photon in the cavity, the quality of lasing emission with a small dephasing is much better than that without dephasing by judging from the clamping of $g_2(0) = 1$. As is missing in the small detuning but no dephasing condition, the clamping of $g_2(0) = 1$ with a dephasing rate of $\delta = 2g$ in a small detuning condition is a clear signature of the onset of lasing. Our calculation shows that the pure dephasing is able to restore lasing in presence of detuning, offering exciting perspective for solid-state nano-laser devices.

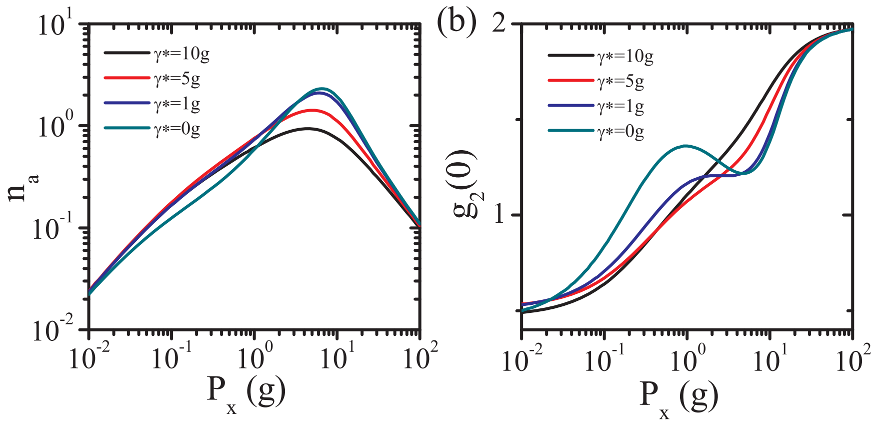

Figure 3.8: Numerically calculated (a) cavity population. (b) statistics of the emitted field as a function of pumping rate in a small detuning condition ($\delta = 2g$), for different dephasing rates.

3.3 A highly efficient single-photon source

An efficient solid-state single-photon source is highly demanded in the context of quantum communication, optical quantum information processing and metrology. Only around 1% emission from single QDs sitting in the bulk material can be collected by an optical lens since the direction of the spontaneous emission is random and most of the emitted light is confined in the high refractive index material due to the total internal reflection. Placing QDs in a naoncavity can efficiently funnel the QDs spontaneous emission into a single cavity mode. The far-field pattern of such a cavity mode can also be very carefully designed to match the optical elements, e.g., optical lens and optical fibers. The spontaneous emission rate to the cavity mode can be dramatically enhanced with a factor of F_p, referred as Purcell factor, which is proportional to $\frac{Q}{V}$. Here, Q and V are the quality factor and mode volume of the cavity respectively. The high Q-factors and extremely low mode volumes of PC cavities make them very attractive candidates for harvesting single-photon emission.

We present detailed investigations on a specific L3 cavity, denoted as cavity 1 in the following. The parameters for this cavity are $a = 240$ nm and $r = 60$ nm. Fig. 3.9(a) shows a broad range μ-PL spectrum of cavity 1, which is taken at a cryogenic temperature (T = 10 K) and high excitation power (P = 1.4 mW). In this spectrum, M1-M5 modes with different emission intensities are clearly seen. The highest energy mode is expected to be around 855 nm by considering the lattice parameters of the cavity. However, it is not visible in this spectrum due to the lack of emitters around the mode energy. The emission properties of single QDs are studied under weak excitation conditions, as shown in Fig. 3.9(b),(c). The carriers can be excited from valence band to conduction band by using a laser whose energy is higher than the energy of the GaAs band gap. In this excitation scheme, many carriers are firstly excited and then relax into all the quantum dos in the excitation area. Alternatively, a certain QD can be quasi-resonantly excited by tuning the wavelength of the excitation laser to the higher-order state and the phonon lines of QDs, which enables selectively exciting a single QD. We show two spectra with the same emission intensity of an exciton line denoted as X in Fig. 3.9(b),(c). To achieve the same emission intensity for the exciton line, the aboveband excitation power is 50 nW five times higher than 10 nW for the quasi-resonant excitation. The spectrum with quasi-resonant excitation is much clearer and only a few emission lines can be observed. We note that this exciton line in the spectra is much brighter than the average emission intensity of the QDs in our samples.

It is very interesting and worthwhile to investigate the total collection efficiency of this dot after the first collection lens denoted as ϵ. We first measure a bulk QD and estimate the total loss of the setup by using the expected counts of bulk QDs after the first collection lens, which is a microscope objective in our setup with a numerical aperture NA = 0.6. The efficiency of a bulk QD in a GaAs matrix is estimated to be around 0.8% for an objective with NA =0.6 after the first lens (calculated by N. Gregersen, DTU). The total rate of the photons emitted by a single QD is given by the repetition rate of the laser, T_{rep} = 76 MHz. Therefore, a comparison of the collected photons at the avalanche photon diode (APD) with 0.8% of 76MHz gives the total loss of the detection part of our setup, which can be used to estimate the collection efficiency of the investigated bright QD. The lower plot in Fig. 3.10 shows power series of a bulk QD under pulsed excitation and the count rate around the saturation power is about 5300 counts/s, which results in a total efficiency of the setup of $\eta = 8.8 \times 10^{-3}$. The upper plot in Fig. 3.10(a) shows the power series of the efficient QD with a count rate of 293×10^3 at the saturation power. The same

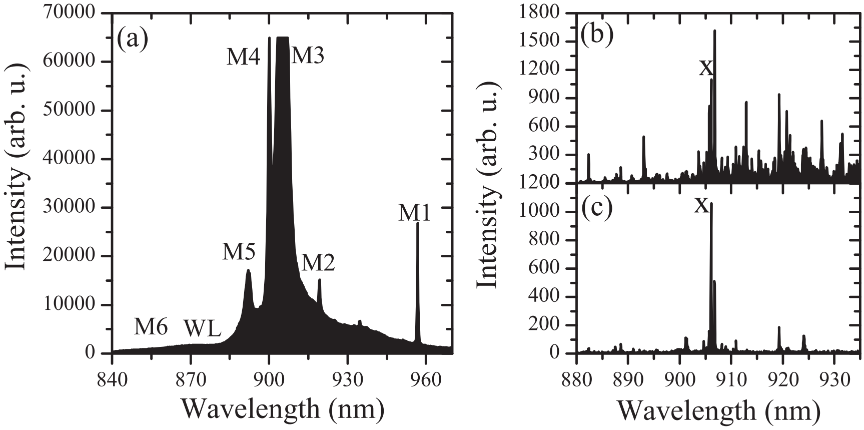

Figure 3.9: Spectra of the QD-cavity system with different excitation powers and methods. (a) Wide range spectrum with high excitation power for detailed investigations of the cavity modes. (b) Narrow range spectrum with low power aboveband excitation. (c) Narrow range spectrum with low power quasi-resonant excitation.

experimental conditions have been used for both power series. Comparing the measured count rate with the total number of emitted photons and taking into account the total loss of the setup, we extract a collection efficiency after the first lens of $\epsilon = 0.38$.

To further confirm the single-photon nature of the emission from our highly efficient QD, a photon statistics measurement has been performed by using a Hanbury Brown and Twiss type interferometer as shown in Fig. 3.10(b). The peak at zero time delay is almost completely missing, which proves a strong suppression of multi-photon emission probability at the measured wavelength. The lifetime of the efficient QD is measured via time-resolved measurements and a fast decay rate of 0.617 ns^{-1} is extracted in Fig. 3.11.

In this sample, we systematically observe efficient QDs ($\epsilon > 0.1$) emitting around the M3 mode, which indicates that such high efficiencies might relate to the coupling between QDs and the M3 mode. We find the Q-factor of the M3 mode is usually around 500 much lower than that of M1 mode. On the other hand the frequency resonance between QDs and M3 mode is easier to satisfy due

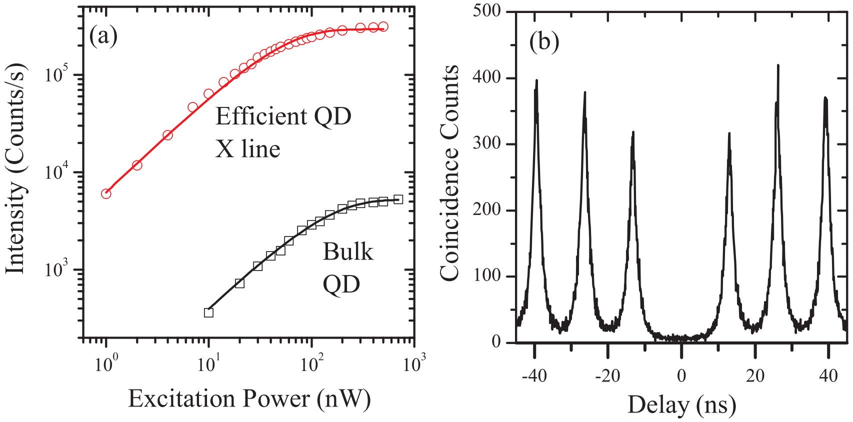

Figure 3.10: Highly efficient single-photon emission from a QD in a PC cavity. (a)Power series of the emission from a bulk QD and the X line of the efficient QD under pulsed excitation conditions. (b) Auto-correlation of X emission line of the efficient QD around the saturation power, showing almost perfect single-photon generation.

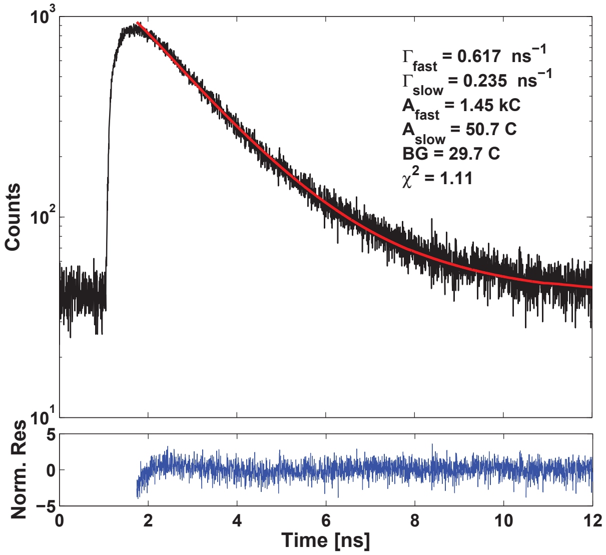

Figure 3.11: Decay curve of the X line of the efficient QD from time-resolved measurements.

to the wide spectral bandwidth of low Q cavity. The mode volume of the M3 mode is relatively large, which enables a better spatial match between the QDs and the cavity mode. We suggest such high efficiencies observed in our sample might originate from the coupling between the QDs and the M3 mode. We further measure many QDs around M3 mode in different cavities to obtain the statistics of the collection efficiency. Fig. 3.12(a) shows the dependence of the collection efficiency on the detuning between the QDs and the M3 mode. The efficient dots are statistically clustered around the long wavelength shoulder of the M3 mode. On the far detuing range of 25 nm away from the the M3 mode, collection efficiencies between 0.1 and 0.2 are observed because at this range the QDs are frequently deep in the PC band gap and the spontaneous emission to guiding modes in plane is strongly inhibited. The QDs can entirely couple to the free space modes, resulting in a greatly enhanced collection efficiency.[55, 56]. The dependence of the decay rate of QDs on the dot-cavity detuning is shown in Fig. 3.12(b). The decay rates of QDs with small detuning are generally faster than those with far detunings. However, we find the frequency range of the enhanced decay rates is wider than the bandwidth of the cavity mode, which could be attributed to the phonon effects[57]. In summary, we find that the highly efficient dots are generally close to the M3 modes and lifetime measurements show a wide coupling range of QDs to the M3 modes. It is also worth to mention that the intensity of M3 mode is generally higher than other cavity modes in our measurements, which indicates the far-field of M3 mode matches the collection objective very well. We believe that the coupling to the M3 mode might be the physical mechanism behind the high efficiencies we observed and more investigations are needed to map the far-field pattern of the M3 mode in the future.

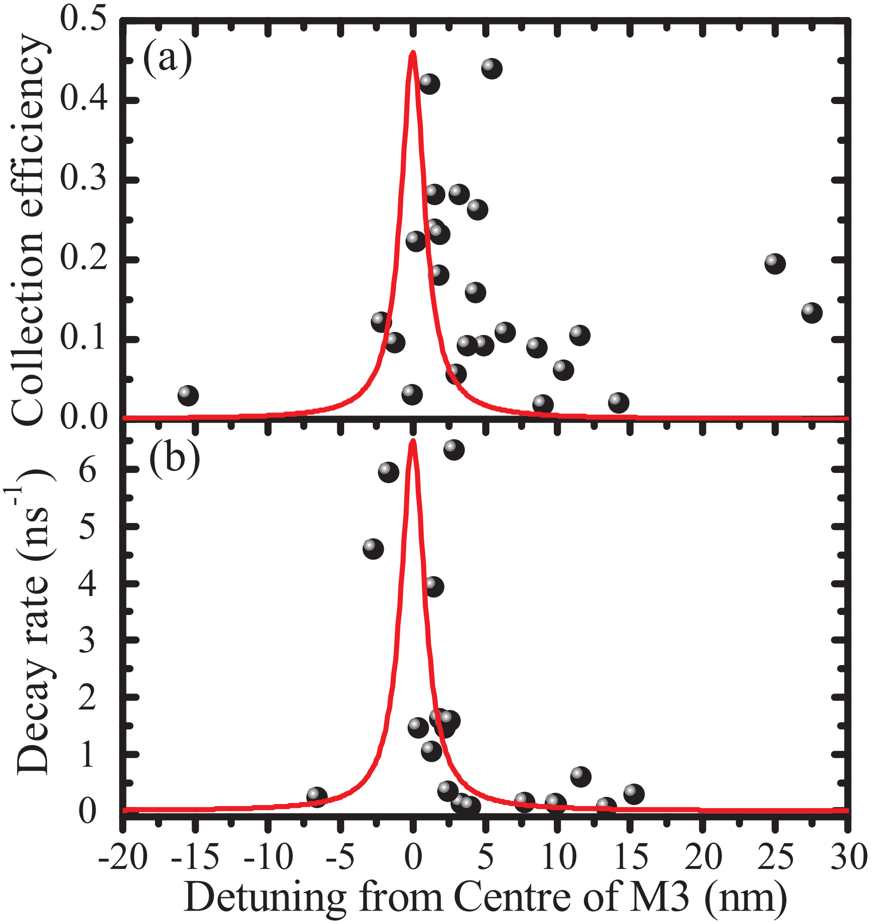

Figure 3.12: The statistical measurements of the collection efficiency (a) and decay rate (b) as a function of dot-cavity (M3) detuning. The point to point fluctuations are expected due to the different spatial matching between QDs and cavities. Red line represents the spectrum of the M3 mode while the black dots are the measured data.

3.4 Few quantum dots lasing in photonic crystal nanocavities

The laser is one of the greatest inventions in the last century and it has been used widely in both scientific research and industry. With increasing advances of modern nanofabrication and understanding of the optical properties of semiconductors, laser devices have been constantly shrinking in size and increasing in efficiency. However, there is a need to further reduce the size of lasers to make them competitive in size and cost to the existing electronic devices and to utilize their potential and unique properties in a wide range of applications. As we discussed before, a high-quality PC cavity efficiently funnels the spontaneous emission from QDs in to a single cavity mode, which enables a smooth transition from spontaneous emission to stimulated emission, referred to as zero threshold lasers[58].

We investigate the laser emission from the fundamental mode of another L3 cavity called cavity 2. We resonantly pump the sample via the highest cavity mode M6 since this method has been demonstrated as an effective way of exciting the QDs spatially sitting in the cavity[59, 60].

Fig. 3.13(a) presents the integrated output intensity and the linewidth of the cavity mode as a function of the excitation power. In regimes I and III , the output intensity increases linearly with the input power. A smooth nonlinear increase of output power can be clearly traced in regime II, which is the signature of onset of high-β lasing. The linewidth of the cavity modes decreases with the excitation power and a plateau has been found in the transition regime. This plateau, regarded as a unique feature of QDs lasers[58], has been observed in similar systems by a few groups[61, 62] although its origin is yet not fully understood. Here we stress the high-quality of our experimental data. Since the phase transition of a high-β laser is very smooth, it is very important to measure and record the output intensity in a stable way. Our samples are placed on a cold finger in a flow cryostat (Oxford Microstat HiRes II). One of the main drawbacks of this flow cryostat is that the samples drift with time in a timescale around 15 minutes. Even a slight drift of the sample will give rise to a significant change in the recorded output intensity, which will blur and even destroy the smooth transition in the data set. One way to overcome this obstacle is to measure only a few data points in a short time

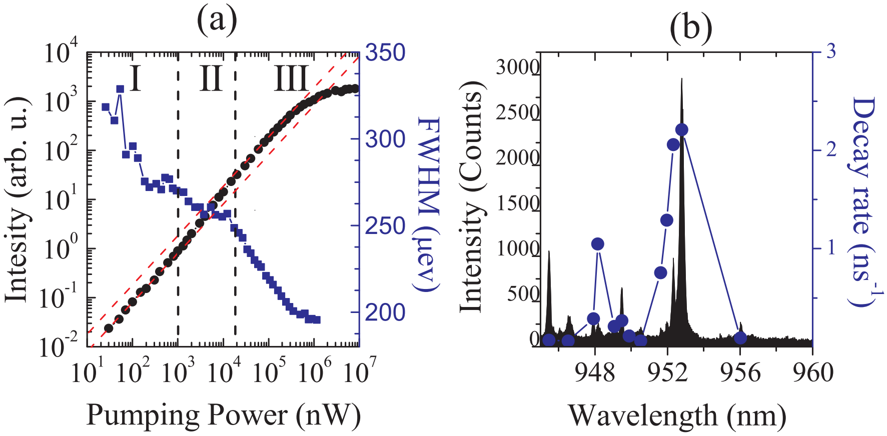

Figure 3.13: Lasing emission from QDs in a PC cavity. (a) The output power (black circles) and the linewidth (blue squares) of the cavity mode as a function of excitation power. Red lines are guides to the eye for a linear increase of output power with a slope of one. (b) The emission spectra (black) of QD-cavity system for 100 nW pumping power and decay rates (blue circles) for different wavelengths.

scale before the drift of the sample. However, it will be very hard to extract any meaningful information of a smooth transition from very limited data sets. In our experiment, the drift of the sample can be monitored by checking the emission intensity of the cavity mode under the lowest excitation power. The best optimized intensity of the cavity mode is used as a drift reference. Before changing the excitation power, we go to the lowest excitation power to check if the cavity output intensity is up to our expectation. If not, we optimize the sample position with a piezo nanopositioner by monitoring the cavity emission intensity and then we immediately increase the excitation power to get a data point. This process has been repeated many times and finally we get 44 points in the data set ranging 5 orders of magnitude in excitation power.

The low excitation power spectra centered at the cavity mode with a range of 20 nm is shown in Fig. 3.13(b), where the discrete exciton lines together with the cavity mode can be clearly identified. By measuring the decay dynamics of QDs and the cavity mode, we found that only four QDs have decay rates comparable to the cavity mode and decay rates of the rest of the QDs in the spectra are strongly inhibited by the photonic band gap effect. Thus, it would approve that only four excitons couple to the cavity and thus contribute to the lasing transition, but as we shall see, it is very hard to directly compare our experimental data of the QD lasers to the single atom laser model due to the following facts. First, there are 4 excitons coupling to the cavity instead of a single exciton. Second, although a QD is referred as an artificial atom, it consists of thousands of atoms thus exhibits mesoscopic features e.g., multi-exciton states under a high excitation power. Last but not the least, the QDs are sitting in a solid environment where the lattice vibrations referred as phonons interact strongly with QDs. Phonons can cause the dephasing and also assist the carrier relaxation process. Thus, a more advanced theory including more physical processes in the QDs is highly needed to model and quantitatively understand our experimental data. A collaboration is established between our group and DTU nanophotonics theory group on the purpose of getting deep understanding of our experimental results on the nanolasers. A semiconductor micro-cavity laser theory developed by our collaborators[63] has been used to model our input-output data. In this model, the lasing emission only originates from the radiative recombinations of the exciton state. Part of the Coulomb interaction (Coulomb interaction between two carriers) is included. Pauli blockage is also implemented so that the population of the exciton state saturates with the excitation power.

We have independently measured all the parameters needed for the modeling with the semiconductor micro-cavity laser theory. The number of QDs and the Q-factor of the cavity can be obtained from the low power spectrum while the coupling strength between the emitters and the cavity can be derived from the measured decay rates in Fig. 3.13(b). In Fig. 3.15, the red solid line is the input-output curve predicted by the theory with measured parameters, which is far from our experimental data. We then try to fit our experimental data by using the number of QDs as a free parameter. With the increasing of the QD number, the fitting starts to approach the experimental curve and finally a very good agreement is achieved by using 120 QDs. In order to understand the discrepancy of the QD number between the experiments and the theory, a high excitation power spectrum is plotted in a logarithmic scale in Fig. 3.14(a). Apart from the cavity mode, a constant background emission has been observed. The

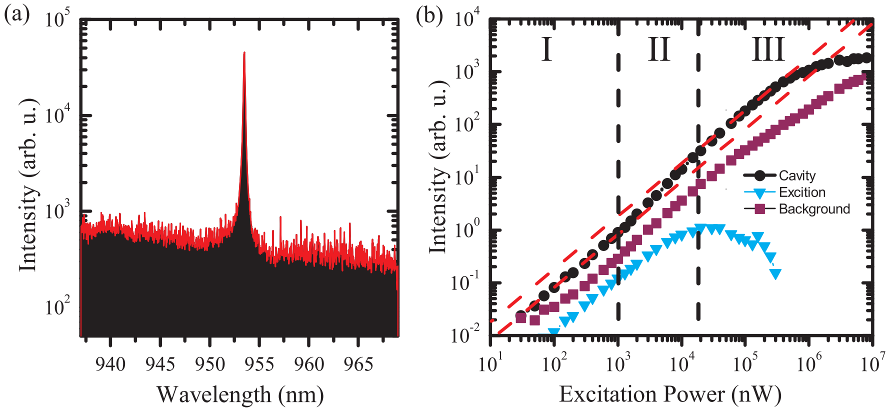

Figure 3.14: (a) High excitation power spectrum in logarithmic scale where the background emission can be clearly seen. (b) Power series of the cavity mode, exciton line and the background emission.

broad background emission is attributed to the multi-exciton states under high excitation powers. In Fig. 3.14(b), the emission intensities of an exciton state, background emission and the cavity mode have been plotted as a function of the excitation power. The exciton emission increases linearly with the excitation power before the saturation while the background emission increases linearly all the way with excitation power. Only the cavity mode shows a nonlinear increase of the intensity with the excitation power, showing that lasing has been achieved. Since the exciton emission saturates around the laser threshold power, it is very unlikely that the lasing is supported by the exciton state of QDs. On the contrary, the very broadband background emission which can be easily resonant with the cavity mode is keeping on increasing above the lasing threshold power and feeds the laser mode.

In our modeling, only the exciton transition is responsible for the laser emission. So the 120 QDs used in the model actually means that 120 exciton states feed the cavity mode. We can think in a way that the extra 116 excitons (only 4 excitons feed the cavity mode concluded from the decay measurement) are playing the same role as the background emission from multi-exciton states in the experiment. In conclusion, we have realized a few QDs lasing in PC nanocavities. Our measurements indicate that the QDs laser is fundamen-

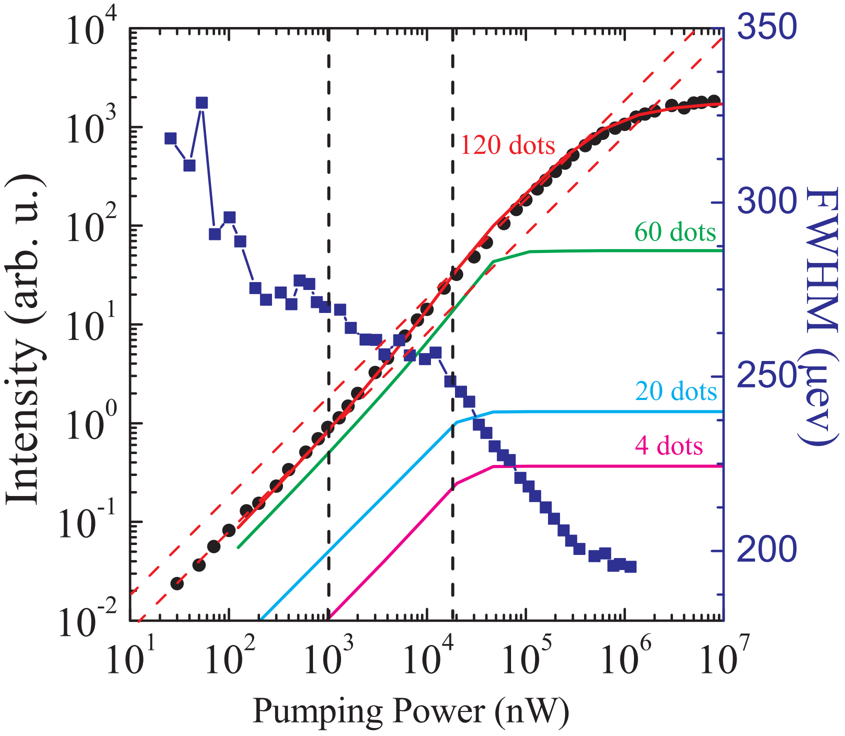

Figure 3.15: Comparison between experimental data and semiconductor microcavity laser theory. The solid lines are the theoretical input-output curves with different numbers of QDs.

tally different from a single atom laser where the atomic transition should be resonant with the cavity mode. Due to mesoscopic nature of the QDs, the broadband multi-exciton states can be easily resonant with the cavity mode and contribute to the lasing. This feature enables a self-tuning mechanism for the gain media, which is very attractive for the device applications.

3.5 Conclusion and outlook

We have theoretically investigated the interaction between a single artificial atom and cavity mode with the aim of understanding a single-QD laser. Based on this model, the prerequisite for a single artificial atom laser has been identified and our calculation suggests that single artificial atom laser is achievable with state-of-the-art fabrication technology. The pure dephasing is implemented in this model and it is shown as a resource instead of nuisance for lasing in the condition of a small detuning between the atom and cavity mode, which indicates a supplementary degree of freedom as compared to isolated atoms, showing great potential for depahsing-controlled solid-state optoelectronic devices. A highly efficient single-photon source based on QDs in PC cavities has been demonstrated and the physical mechanism is suggested as the coupling between the QDs and one of the higher cavity modes. We also observe high-β lasing emission in the same system and the comparison to a more advanced theory reveals the fundamental difference between QDs and atom in the context of lasing emission. In the future, a calculation of the far-field pattern of the higher order mode of PC cavities is highly desirable for understanding such high collection efficiencies in our experiments. Our lasing experiment calls for more advanced theories including multi-exciton states in order to understand the physics of QD lasing.

Chapter 4

Anderson-localized random lasing

In this chapter, systematical investigations on random lasers in PCs waveguides have been presented. We have shown a fundamentally different approach in which disorder is utilized to enhance light-matter interaction. Random lasing with Anderson-localized modes in PC waveguides has been observed. The lasing wavelength is determined by the band edge of the waveguide modes, which provide a possibility of tuning the lasing wavelength in a wide range. The random lasing can be very well described by a modified semiconductor laser rate equation. The statistical properties of random lasing in Anderson localization have been studied to understand random lasing dominated by multiple scattering processes.

4.1 Introduction

4.1.1 Multiple scattering of light

Light is multiply scattered along different directions when propagating in a disordered media. A complex spatial intensity profile, e.g., laser speckle is generated due to interferences of the different possible light path inside the disordered media. After ensemble averaging the over all statistical realizations of the disorder, interference is usually negligible and the light transport can be approximated as a diffusion process. On the other hand, if multiple scattering is very pronounced wave interferences can lead to new physics. The most prominent example is the formation of Anderson-localization of light. In Anderson-localization regime interference causes large fluctuations in the spatial intensity profile while its ensemble-averaged envelope decays exponentially away from the light source. As a consequence, light is confined by disorder on a typical length scale called localization length, ξ. Fig. 4.1(a) shows an example of probing light localization by placing an emitter in an one-dimensional stack with different refraction indexes with a random manner[64]. One dipole emitter is placed in the center of the stack. Fig. 4.1(b) is the intensity distribution for the light emitted by the dipole and this distribution could be random for a single disorder realization. After an ensemble average of many realizations, the intensity drops exponentially with the distance to the emitter, shown in Fig. 4.1(c). Anderson-localization was firstly introduced by P. W. Anderson to explain the localization of electrons[65] in a random potential but later has been observed universally exist in light[7], sound[66] and matter waves[67]. In three-dimensional system a phase transition between diffusion and localization is expected when the average distance between two scattering events, is smaller comparable to the wave number. In lower dimensions a crossover takes place from ballistic or diffusive light to localization. Anderson localization occurs in an one-dimensional random media on the condition that the sample length, L, exceeds the localization length.

4.1.2 Random lasing

Tightly confining light at nanoscale is a crucial task in modern nanophotonics. To date, it has been widely realized by carefully designing various optical microcavities[68]. Anderson-localization offers a brand new way of confining light at nanoscale in the context of enhancing light-matter interactions and nanophotonic devices. Among all possible applications of devices based on multiple scattering, random lasing shows great potential for imaging[69] and sensing[70] etc and it is easy to realize due to its robustness against disorders. Initially suggested by Letokov[71] in the sixties and experimentally realized for the first time by Lawandy[72] and co-workers, a random laser is basically the combination of elastic scatters and a gain media. In a conventional laser, the light amplification is generated by a combination of a gain media and optical

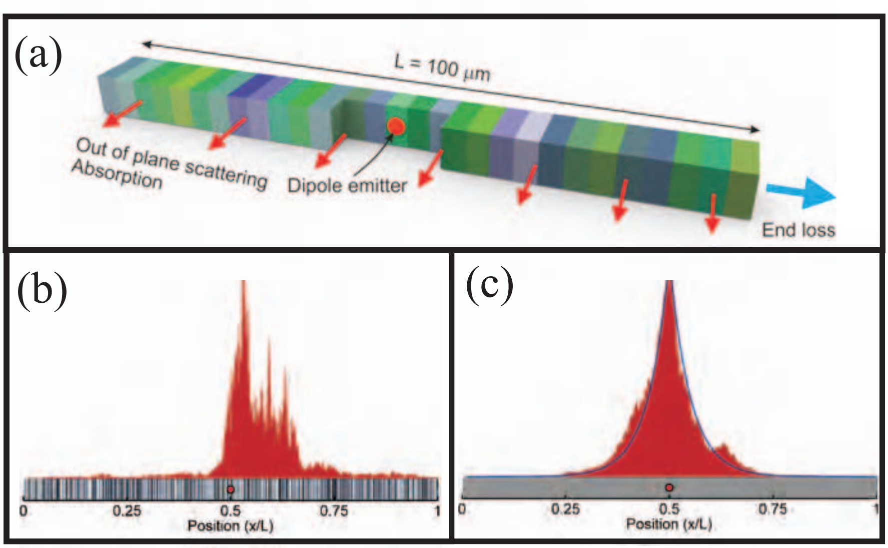
(a)
L = 100 μm
Out of plane scattering
Absorption
Dipole emitter
End loss
(b)
0
0.25
0.5
0.75
1
Position (x/L)
(c)
0
0.25
0.5
0.75
1
Position (x/L)

Figure 4.1: Light localization in an one-dimensional stack. (a) The sketch for an one-dimensional stack with a dipole sitting in the center. (b) Calculated intensity profile of the light emitted by the dipole. (c) Ensemble-averaged intensity profile. *Figure by courtesy of H. Thyrrestrup.*

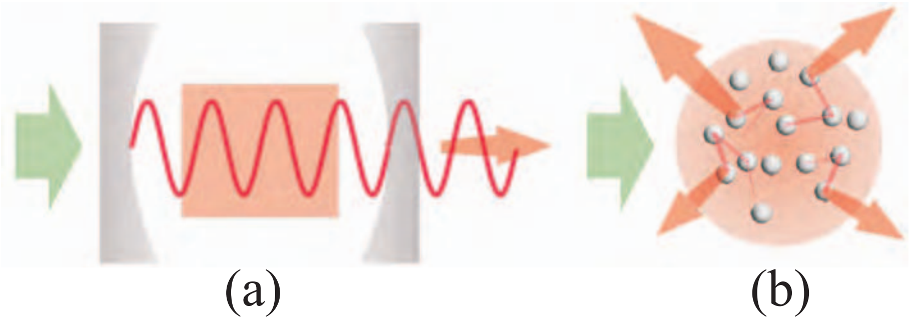

Figure 4.2: A comparison between conventional lasers and random lasers. (a) A conventional laser is composed by a gain medium and an optical cavity which provide the necessary resonant feed back to achieve stimulated emission. (b) A random laser system in which the light is amplified by multiple scattering, the random laser modes are defined by eigenmodes supported by the random media. *Figure by courtesy of P. D. Garcia.*

cavity. In this coherent amplification process, light scattering hampering the functionalities is generally regarded as a nuisance to minimize. On the contrary, the multiple scattering process gives rise to the feedbacks (resonant and non-resonant) for achieving lasing oscillations in a random media. shown in Fig. 4.2. Random lasers are profusely found in diffusive regime however the its physical mechanism is still under debates. From the viewpoint of enhancing light-matter interaction at nanoscale, random lasing in Anderson-localization is highly needed since the light is much strongly confined in localization regime than diffusion regime.

4.1.3 Anderson-localization of light in photonic crystal waveguides

Reaching Anderson-localization of light in three-dimensional random media is extremely difficult and no control can be exerted over the frequency or spatial extent of the localized modes. A promising proposal on how to control multiple scattering is to induce a slight amount of disorder in periodic nanostructures[11] in which the light propagation is described by Bloch modes. Breaking the symmetry of such structures leads to multiple scattering of light and gives rise to light localization. Due to the highly dispersive optical DOS in PCs, light localization can be spectrally controlled by engineering the band structures. The first experimental signature of light confinement in disordered photonic crystal waveguides was shown by J. Topolancik and co-workers[73]. Close to the waveguide mode band edge, they observed spatially confined modes appeared near to the band edge of the waveguide modes. These modes have been later unequivocally demonstrated as a result given by Anderson-localization of light by statistical measurements[64]. These localized modes have been further shown as an alternative of PC cavities in the framework of solid-state quantum electrodynamics[74].

4.2 Random lasing in photonic crystal waveguides

4.2.1 Sample characterizations

In the following of this chapter, we will show how to employ these localized modes to achieve localized random lasing and statistical properties of the localized random lasing. Our samples are InGaAsP membranes containing 10 layers of 5-nm-thick InGaAsP quantum well in the center. An ordered triangular lattice of holes is etched in the structure creating a 2D photonic band gap that suppresses in-plane propagation of light and the waveguide is formed by leaving a single row of the holes as shown in the scanning electron microscope image in Fig. 4.3(a). We investigate a set of PCWs with length 100 µm, membrane height $h = (340 \pm 5)\,\mathrm{nm}$, a lattice constant $a = 380\,\mathrm{nm}$ and a range of different hole radii $0.237a < r < 0.263a$. Imperfections in the PCW lead to multiple scattering of light thus inducing localized modes in the high optical density of the states (DOS) regime if the sample length exceeds the localization length and light losses are negligible[75]. In the present case, unavoidable disorder is originated in the fabrication process which has been observed to be sufficient to lead to Anderson-localization [64]. We optically characterize our system by using a confocal micro-photoluminescence setup to excite the quantum well and collect the emitted light within a diffraction-limited region. Photoluminescence emission spectra are collected in a wide wavelength range $1500\,\mathrm{nm} - 1600\,\mathrm{nm}$ with a spectrometer (0.1 nm resolution) equipped with an

InGaAs CCD camera while scanning the excitation and collection objective along the PCW, as shown in Fig. 4.3(b). The figure reveals the modes spatially localized along the waveguide and spectrally distributed in the high-DOS regime. We numerically investigate these Anderson-localized modes by simulating a 100 μm long PCW where disorder is induced by randomly varying the hole positions according to a Gaussian distribution with standard a deviation of δ=1%. Fig. 4.3(b) shows the spatially confined electric field after exciting the structure with a broadband source centered at the high-DOS regime of the unperturbed structure. When the waveguide is pumped with a power above the laser threshold, clear lasing modes are observed along the PCW which spectral position strongly depends on the r/a value, as shown in Fig. 4.3(d). Random lasing in the Anderson-localization regime can be spectrally tuned along the full fluorescence spectrum of the quantum well within almost 300 nm, showing a much broader spectral tunability than diffusive random lasers [76, 77].

4.2.2 Single- and multi-modes random lasing

Random lasing in disordered PCWs operates in single- and multi-mode regime, as shown in Fig. 4.4. Fig. 4.4(a) plots the output fluorescence intensity vs. excitation power for a single lasing mode. The so-called input-output curve exhibits a typical threshold behavior which we fit with a modified laser rate equation (explained later), accompanied by a decrease of the linewidth cavity mode, as a clear signature of laser oscillation. As a reference, we show how the background quantum well fluorescence intensity increases linearly with the excitation power. Fig. 4.4(b) depicts the fluorescence spectra below and above the lasing threshold corresponding to the excitation power marked by the arrows in Fig. 4.4(a). The insets show optical microscope images of the area measured in the PCW below and above threshold. In addition to this single-mode lasing, we observe multi-mode lasing as shown in Fig. 4.4(c) and (d). The input-output curves plotted in Fig. 4.4(c) show a different behavior for each of the individual lasing modes fitted with the modified laser rate equation (explained later). Although a clear multi-mode operation is observed, no mode competition is revealed in Fig. 4.4(d) where the input-output curve of a particular laser mode is independent of subsequent lasing modes. This reduces complicating chaotic lasing effects typical of diffusive random lasers10 and may be use to drive the random laser to a regime of collectively oscillating strongly

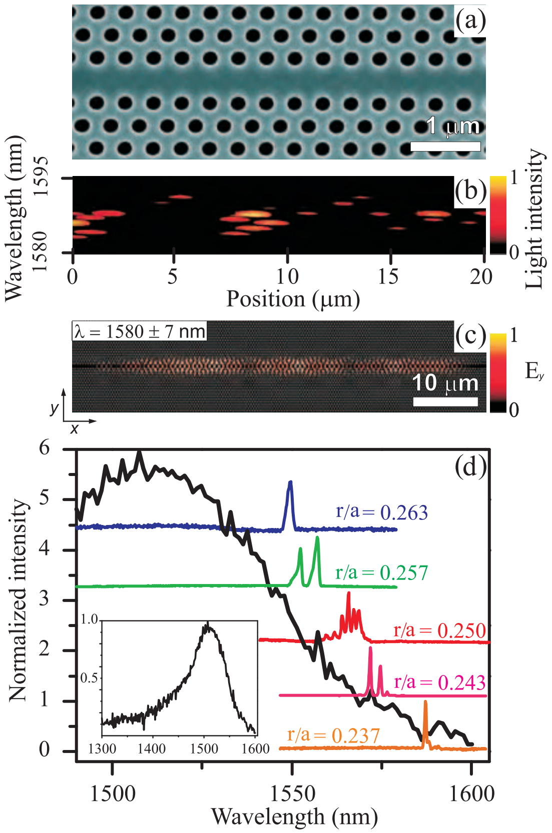

Figure 4.3: **Random lasing in the Anderson-localization regime.** (a) Scanning electron microscope image of a PC waveguide (PCW). (b) Photoluminescence intensity under an excitation power of 500 μW collected while scanning the excitation and collection objective along a PCW. (c) 2D finite-difference time-domain calculations of the y component of the electromagnetic field in a disordered PCW with $r/a = 0.28$ and $\delta = 1\%$ showing strongly confined Anderson-localized modes in high-DOS regime after exciting the structure with a broadband source centered at 0.26 (a/λ) with a bandwidth of 0.02 (a/λ). The intensity of the y-polarized electric field is plotted on top of the simulated structure. (d) Photoluminescence spectra vertically shifted for visual clarity under excitation power above lasing threshold collected for various values of r/a. The quantum well fluorescence spectrum is shown for comparison (black line). The inset shows the full quantum well spectrum.

interacting modes,required for mode-locking operation[78].

Lasing due to multiple scattering is ultimately a random process that requires a statistical description. Fig. 4.5(a) and (b) present the statistical distributions of Q-factor and threshold power directly obtained from our measurements. The Q-factor distribution is measured at the excitation power at which the lasing mode appears and it is compared with a recently developed 1D model that enables us to determine the localization length and the loss length of the system[64]. From this comparison, we extract a localization length of $\xi = 6\,\mu\text{m}$ which is much smaller than the sample length $100\,\mu\text{m}$ thus confirming Anderson-localization in our system. From the distribution, we also extract an average loss length of $l_\sigma = 800\,\mu\text{m}$. By extrapolating the input-out curves shown in Fig. 4.4(d) to zero excitation power, we obtain a distribution of the random lasing threshold. The average threshold obtained here is similar to the typical threshold of PC nanocavity lasers at room temperature ($200\,\mu\text{W}$)[79], which indicates the potential of random lasing for device applications. In addition, we fit our experimental threshold distribution with a theoretical model developed to explain random lasing considering random resonators [80] in which the threshold distribution function, $F(I_{th})$, is given by the relation

$$F(I_{th}) = \frac{\beta_0}{I_{th}}(\frac{I_{th}}{I_t})^{\beta_0}\exp[-(\frac{I_{th}}{I_t})^{\beta_0}] \tag{4.1}$$

where β_0 is a dimensionless parameter that is inversely proportional to the amount of disorder of the system, I_{th} is the excitation threshold intensity and I_t is the average threshold intensity. The asymmetric threshold distribution shown in Fig. 4.5(b) presents a long tail towards high threshold values in contrast to the symmetric threshold distributions observed in weakly scattering materials[81]. This behavior is predicted by the model for strongly scattering systems and is confirmed buy the value of β_0 extracted from the fitting, 2.1, much smaller than the value obtained in the mentioned weakly scattering case. Quite remarkably, the broad and asymmetric threshold distribution measured here strongly supports the model of random resonators as the main mechanism behind random lasing[80].

4.2.3 Modeling Random lasing

Conventional semiconductor lasers have been widely modeled with the laser rate equation[82]. In our case, we model random lasing with a modified micro-

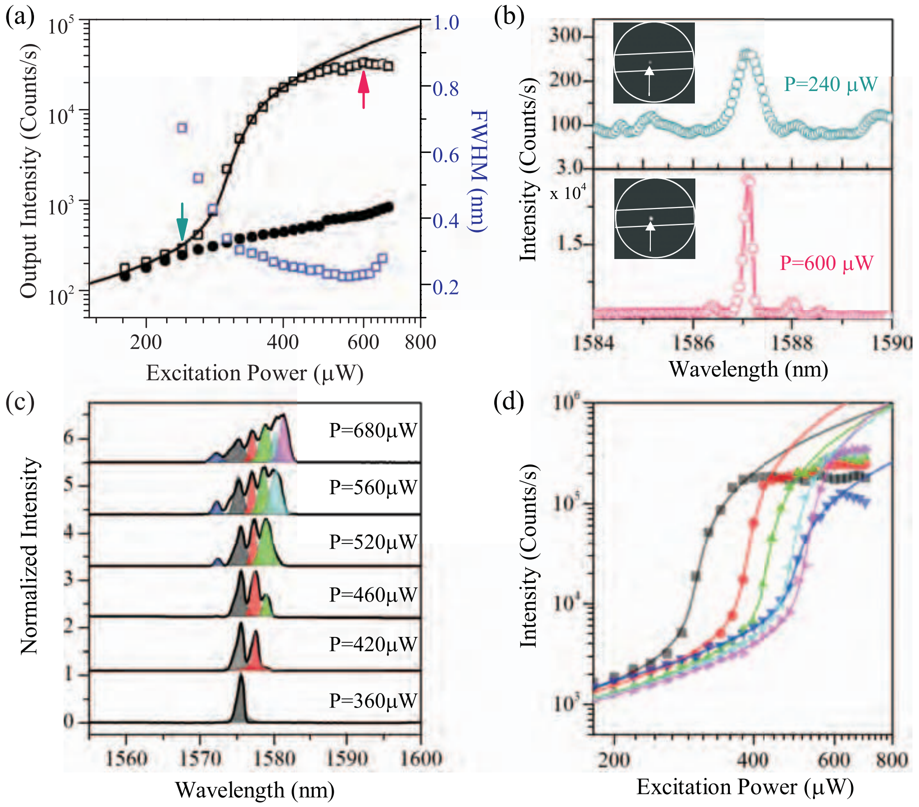

Figure 4.4: **Single- and multi-mode operation of random lasing in the Anderson-localization regime.** (a) Output intensity (black squares) and linewidth (blue squares) of a single lasing mode vs. excitation power. The solid line represents the fit to a modified semiconductor laser rate equation. The black dots represent the background quantum-well fluorescence. The arrows indicate the excitation power of the spectra shown in (b). (b) Photoluminescence spectra of a single mode below and above the lasing threshold. The insets show optical microscope images of the emission. (c) Photoluminescence spectra vs. excitation power for different lasing modes in multi-mode operation. The different colored curves are fits with Lorentzian curves representing different lasing modes. (d) Photoluminescence intensity vs. excitation power for multi-mode operation where mode competition is clearly observed. The solid lines represent the fit to the semiconductor laser rate equations for each lasing mode.

cavity laser rate equation due to the existence of random resonators induced by Anderson-localization. When placed in a micro-cavity, the spontaneous emission from a semiconductor QD is enhanced with a Purcell factor proportional to $\frac{Q}{V}$, where Q is the cavity quality factor and V is the cavity mode volume [68]. A recent theoretical investigation suggests that the contribution of the cavity quality factor can be neglected in the case of quantum wells due to the mismatch between the optical and the electronic density of the states[83]. However, this situation becomes even more complicated when the mode volume of a cavity is comparable to the volume of the gain material, as in our case. It requires the modification of the conventional optical confinement factor $\Gamma = \frac{V_{\mathrm{a}}}{V}$[84], where V_{a} is the the active material volume and V is the laser cavity mode volume. By taking these factors into account, we develop a modified semiconductor laser rate equation to fit our experimental input-output lasing curves (see appendix). By doing so, we fix all the material parameters and leave β, the fraction of spontaneous emission that seeds the laser process, and V as free fitting parameters. Fig. 4.4(a) and (c) show a very good agreement between the experimental data and the fitting with our model. The saturation and mode competition effects are not included in the current model due to the complexity of the hole-burning effect and thermal effect in our room temperature experiments. Fig. 4.5(c) and (d) show the distributions of the β factor and the mode volume obtained by fitting all the measured input-output curves. Fig. 4.5(c) presents the β factor distribution which ranges from 0.28 to 0.38, significantly higher than those corresponding to PC micro-cavity lasers with quantum well as gain material (0.09-0.15)[85, 79]. The mode volume shown in Fig. 4.5(d) ranges from 4 to 6 $(\lambda/\mathrm{n})^3$, in agreement with predicted mode volumes for this systems[86]. The mode lengths are calculated by dividing the mode volumes with an effective transverse mode area $\mathrm{A}_{\mathrm{eff}}$, shown in the top horizontal axis in Fig. 4.5(d). In order to calculate $\mathrm{A}_{\mathrm{eff}}$ we take the measured parameters of the PCW. The field distribution for the zero order waveguide mode at the band edge for an ordered waveguide is calculated with the MPB software and, averaging over one unit cell along the waveguide, we obtain a value of $\mathrm{A}_{\mathrm{eff}} = 0.11\,\mu\mathrm{m}^2$. The calculated mode lengths are close to the localization length extracted from an independent Q-factor measurement, showing consistency between different measurements. The full statistical description shown here and the agreement with our model of micro-cavity laser strongly supports the existence of random resonators as a mechanism for random lasing in disordered PCW.

4.2.4 Controlling light localization with gain

So far, Anderson-localization has been mainly probed in transmission experiments by measuring the intensity of an external light source after propagation through a disordered medium. In such a configuration, discriminating between Anderson-localization and simple absorption constitutes a major challenge. To overcome this, the variance of the transmitted intensity was proposed as a criterion for Anderson-localization even in the presence of weak absorption[87]. Alternatively, the use of quantum emitters embedded in the disordered structure extraordinarily improves this analysis since it allows to efficiently excite even the most strongly localized modes[64], hardly accessible with an external light source. In this context, a dramatic increase in the losses may destroy the confinement of light due to Anderson-localization. On the contrary, optical gain compensates the effect of light losses thus recovering the confinement of light. To analyze this quantitatively, we measure the probability distribution describing the intensity fluctuations $P(\widehat{I} \equiv I/\langle I \rangle)$ along the PCW, plotted for different excitation power in Fig. 4.6. $P(\widehat{I})$ is extracted experimentally from the photoluminescence spectra collected at different positions while scanning the sample with a confocal microscope. Under low excitation power, all the localized modes are well below the laser threshold as shown in Fig. 4.4(d) and experience a strong absorption due to the 10 quantum well layers. In this configuration, $P(\widehat{I})$ presents a normal distribution plotted in Fig. 4.6. On the contrary, by increasing the excitation power, light amplification compensates absorption leading to random lasing for which $P(\widehat{I})$ presents a typical log-normal distribution characteristic for Anderson-localization [87]. The variance of the intensity fluctuations, plotted in the inset of Fig. 4.6, monotonically increases when increasing the excitation power. The largest variance of 1.7, observed for the strongest excitation power, is larger than 0.5 which is the required variance for Anderson-localization in one dimensional structures[88].

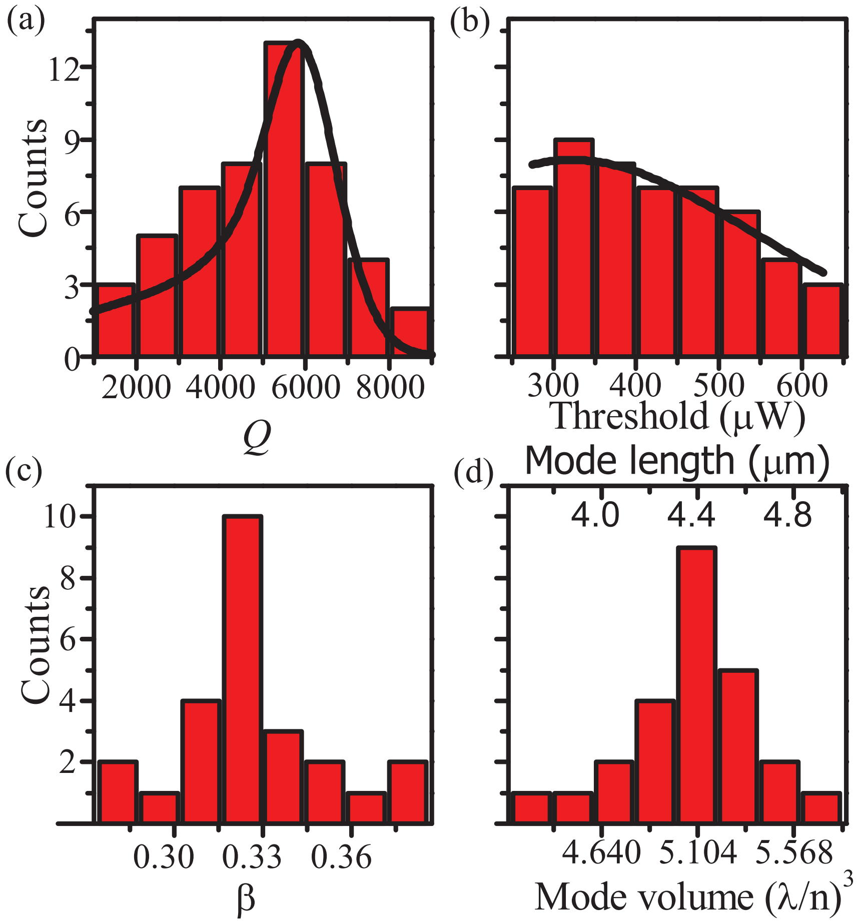

Figure 4.5: **Statistical distribution of lasing parameters for a random laser in the Anderson-localization regime.** (a) Experimental Q-factor distribution of the observed localized modes in the PC waveguide (histograms). Black line is the fitting of Q-factor distribution. (b) Laser threshold distribution obtained by extrapolating the input-out curves shown in Fig. 4.4(d) to zero excitation power. Black line is the fitting of threshold distribution. (c) and (d) β factor, mode volume (converted to mode length in the top axis) distributions extracted by fitting the input-output curves with a modified semiconductor laser rate equation, respectively.

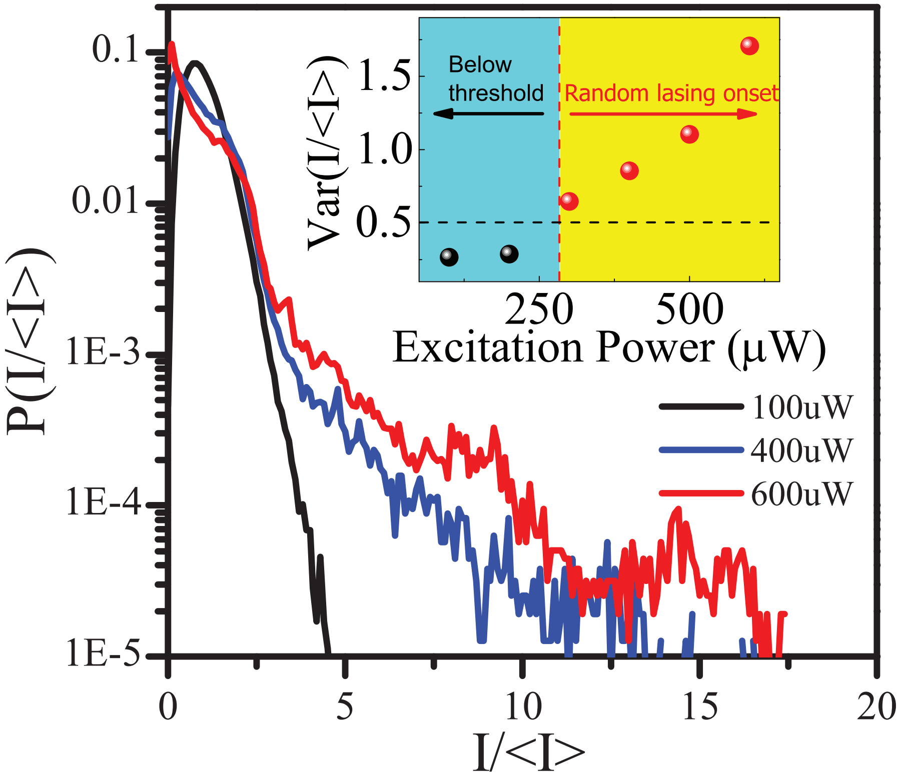

Figure 4.6: **Intensity probability distribution vs. excitation power.** Intensity probability distribution for different excitation powers 100, 400 and 600 μW. The inset shows the variance of the normalized intensity as a function of the excitation power. The horizontal dashed line shows the localization criteria of one dimensional structures, $Var(\widehat{I}) = 0.5$, and the vertical line indicates the excitation power from which the system start to lase.

4.3 Conclusion and outlook

In summary, we observe single- and multi-mode random lasing in PCW deep in the Anderson-localization regime. The lasing modes can be tuned over a very broad wavelength range by engineering the underlying dispersion relation. We present a complete statistical description of random lasing in this transport regime using a modified semiconductor micro-cavity laser rate equation to model the experimental parameter distributions. Our results confirm previous theoretical predictions based on the existence of random resonators as the mechanism behind random lasing. Our analysis paves the way to control and optimize lasing in low dimensional optical nanostructures commonly used for tailoring the light-matter interaction. In the future, engineering a system in which the localization length, absorption (gain) length and the sample length can be controlled to map the complete diagram of light transport in a non-conservative medium will be an extremely interesting task. One of the promising candidates for this experiment could be PC waveguides in which the gain and loss can be controlled by the amount of the embedded gain media and the localization length can be tuned with the amount of disorder.

Chapter 5

Conclusion

This thesis focuses on optical characterizations and fabrication technologies of optically active semiconductor nanomembranes with the emphasis of enhancing light-matter interaction at nanoscale.

One of the central naonstructures used for confining the light tightly at nanoscale is the PC nanomembranes containing internal quantum emitters, i.e., QDs have been fabricated. The fabrication method we developed for PC nanomembranes is based on e-beam soft masks instead of conventional hard masks, which significantly reduces the complexity of the fabrication process and yields state-of-the-art PCs. Also, the fabrication process for GaAs optomechanical nanomembranes has been developed by using two selective wet etch processes. The fabricated nanomembranes shows a world-record mechanical Q-factor up to 1 million, which gives rise to superb performances in cavity optomechanics experiments. Our experiments show that direct band gap semiconductor nanomembranes might bring a new degree of freedom, e.g., coupling light emitted by quantum emitters to the mechanical motions of nanomembranes in cavity quantum optomechanics .

The interaction between single QDs and PC cavities has been systematically investigated in the frame work of JCM in which QDs and cavities are approximated as two-level atoms and single-mode electromagnetic field. Introducing dephasing in the system surpricely recovers the lasing in the presence of a small detuning. This calculations suggest that pure dephasing might be a resource which can be engineered to improve the device performance in solid-state quantum circuits.

We have experimentally demonstrated the quantum light sources, i.e., single-photon sources and nanolasers based on QDs in L3 PC cavities. Bright single-photon emissions are observed in our sample with different filling factors and the brightest exciton line exhibits a collection efficiency up to 38% with a perfect suppression of multi-photon emission. The physic mechanism behind such a high efficiency is suggested as the coupling to the M3 mode of the cavity although more investigations on the far-filed pattern is needed to verify our postulation. Considering the cavity effects in the single-photon emission, an ideal highly efficient indistinguishable single-photon source can be envisioned based on this system.

PC lasers, regarded as ultimate nanolasers have been systematically investigated in our samples. By independently measuring all the parameters needed in the model, we made a quantitative comparison to an advanced semiconductor micro-cavity laser theory and our results show QD lasers are fundamentally different from atom lasers due to the multi-exciton states which are specific to solid-state emitters.

Finally, we have realized nanolasers by using a totally different strategy, i.e., Anderson-localization of light. Instead of showing single lasing devices we perform statistical measurements on this system and model our experimental data with a modified semiconductor laser rate equation. We show that random lasing can be used as an extra degree of freedom to tune our system into and out of Anderson-localization regime.

Appendices

Appendix A

Fabrication procudures

A.1 PC membranes process

This process was developed for fabricating various PC membranes structures, i.e., PC cavities and PC waveguides. It could also be used for optical lithography process by replacing e-beam resist with photoresist.

- **Spin-coating** using a Karl Suss RC8 spin-coater and 11% ZEP 520A resist. Resist distribution. closed spin with 500 rotations per minute (RPM) for 10 s and an initial acceleration of 100 RPM/s. Immediately followed by spin coating: colsed spin with 2000 rotations per minute for 30 s and an initial acceleration of 1000 RPM/s. This results in a resist thickness around 550 nm.

- **Pre-bake** on hotplate at 160 °C for 120 s.

- **Electron beam exposure** using a Jeol JBX-9300Fs e-beam lithgraphy system. Exposure using 100 kV acceleration voltages, current 1 nA, and dose 300 μC/cm^2.

- **Development** in ZED-N 50 for 120 s. Clean in isopropanol. No post-bake.

- **ICP dry etch** using a STPS ICP system with a Ar-flow of 12 sccm, BCl_3-flow of 3 sccm and Cl_2 flow of 4 sccm for 60 s. A nominal platen power of 80 W and a coil power of 700 W were applied. The chamber pressure is maintained at 20 mTorr during the dry etch.

- **Resist removal** in Microposit Remover 1165 heated to 60 °C with the smallest ultrasonic applied for 1 hour. The surface of the surface of the resist forms a chemically very stable polymer compound during exposure to ICP etch, so it is important to start the ultrasonication immediately after the sample has been submersed in the resist remover. Otherwise residues of the surface polymer may adhere to the surface of the GaAs and thus degrade the final device quality.
- **Selective undercut** using 40% HF to release the GaAs membranes.
- **Post-cleaning** with KOH and Oxygen plasma.

A.2 GaAs optomechanical nanomembrane process

- **Spin-coating** using a Karl Suss RC8 spin-coater and AZ5214E resist. Resist distribution: closed spin with 500 rotations per minute (RPM) for 5 s and an initial acceleration of 100 RPM/s. Immediately followed by spin coating: closed spin with 1000 rotations per minute for 30 s and an initial acceleration of 2000 RPM/s. This results in a resist thickness around 3300 nm on the front side of the wafer.
- **Hard-bake** on hotplate at 160 °C for 30 mins.
- **Spin-coating** using a Karl Suss RC8 spin-coater and AZ5214E resist. Resist distribution: closed spin with 500 rotations per minute (RPM) for 5 s and an initial acceleration of 100 RPM/s. Immediately followed by spin coating: closed spin with 2000 rotations per minute for 30 s and an initial acceleration of 4000 RPM/s. This results in a resist thickness around 2300 nm on the back side of the wafer.
- **Hard-bake** on hotplate at 130 °C for 120 s.
- **Ultraviolet exposure** using Karl Suss mask aligner.
- **Development** in AZ351B for 60 s. Clean in H_2O and blow dry.

- **Oxygen plasma** remoing the residues of the photoresist.
- **wet etch** the samples in Citric acid solution.
- **Removing the photoresist** using Microposit remover 1165 at 65 °C for 5 mins and clean.
- **Removing AlGaAs layer** using 10% HF for 10 s.
- **Post-cleaning** with KOH and Oxygen plasma.

A.3 Wedged plasmonic waveguides prcess

- **Clean** sample in acetone, ethanol and isopropanol and blow try.
- **Spin-coat** using a Karl Suss RC8 spin-coater and 3.8% ZEP 520A resist. Resist distribution. closed spin with 100 rotations per minute (RPM) for 10 s and an initial acceleration of 500 RPM/s. Immediately followed by spin coating: colsed spin with 1500 rotations per minute for 30 s and an initial acceleration of 2000 RPM/s.
- **Electron beam exposure** using a Jeol JBX-9300Fs e-beam lithgraphy system. Exposure using 100 kV acceleration voltages, current 1 nA, and dose 300 μC/cm^2.
- **Development** in ZED-N50for 120 s. Clean in isopropanol. No post-bake.
- **Wet etch** in H_2SO_4/H_2O_2 solution for 30 s.
- **Resist removal** in Microposit Remover 1165.
- **Clean** sample in acetone, ethanol and isopropanol and blow try.

Appendix B

Detailed information on random lasers

B.1 Sample fabrication

The semiconductor heterostructure used for the fabrication of the PCWs is grown on a (100)-oriented semi-insulating indium phosphide (InP) substrate by metalorganic chemical vapor deposition (MOCVD). The structure consists of a 340-nm-thick InGaAsP membrane, which is grown on a 100-nm-thick InP, 100-nm-thick InAlAs and 800-nm-thick InP sacrificial layer incorporating 10 layers of InGaAsP quantum well at the center with a thickness of 5 nm and a separation of 5 nm between adjacent QW. The PCWs are fabricated by electron-beam lithography, reactive-ion etching, and wet etching using hydrochloric acid solution and hydrofluoride Acid with lattice constant $a = 380\,\text{nm}$, and a range of different hole radii $0.237a < r < 0.263a$. Finally, 340-nm-thick suspended membranes are formed by removing the sacrificial layer.

B.2 Experimental setup and optical characterizations

Microphotoluminescence measurements are carried out at room temperature. A 120 fs pulsed Ti:sapphire laser operated at 800 nm with a repetition rate of 80MHz is used for optical pumping. An excitation beam is focused to a spot with a diameter of 1.5 μm on the surface of the sample using a 50X microscope objective lens (numerical aperture: 0.65), and positioned on the photonic crystal waveguides using piezoelectric nanopositioners. The photoluminescence signal is collected by the same objective lens within a diffraction-limited region in a wide wavelength range $1500\,\text{nm} < \lambda < 1600\,\text{nm}$, dispersed by a 300 mm grating spectrograph with a spectral resolution of 0.1 nm, and detected using a liquid-nitrogen-cooled InGaAs CCD (charge-coupled device) camera. The intensity probability distribution $P(\widehat{I})$ is measured by collecting the intensity $I^{\lambda}_{x,y}$ while scanning the excitation and collection objective along the PCW at each spatial position (x, y) with a spatial binning size of 0.25 µm and at different wavelengths with a binning size of 1 nm. Subsequently, an average over the wavelength range $1580\,\text{nm} - 1595\,\text{nm}$ is performed.

B.3 Rate equation analysis

We use a modified semiconductor laser rate equation model for the carrier density N and the photon density P of the random laser

$$\frac{dN}{dt} = R_{\text{p}} - BN^2 - \frac{\Gamma^{\text{G}}}{\Gamma}G(N)P - AN - CN^3, \tag{B.1}$$

$$\frac{dN_{\text{P}}}{dt} = \Gamma\beta BN^2 + \Gamma^{\text{G}}G(N)P - \frac{N_P}{\tau_{\text{P}}}, \tag{B.2}$$

where R_{p} is the pulsed injected carrier density with the temporal width of the excitation laser pulse. B is the the bimolecular recombination coefficient of the unstructured material which we assume here to be unchanged by the photonic crystal structure, A and C are the non-radiative coefficients corresponding to surface recombination and Auger processes respectively. Γ and Γ^{G} are the conventional and generalized confinement factors, $G(N) = \text{c}/n_{\text{eff}}G_0(N\text{-}N_{\text{tr}})$ is the gain coefficient, and τ_{P} is the photon lifetime obtained by the measured Q factor near the laser threshold. We assume that the contribution of the cavity quality factor can be neglected in the case of quantum wells since the electronic density of states here is very broadband compared to the cavity bandwidth[83]. Furthermore, the cavity mode volume is comparable to the volume of the gain material, which is the case in the present experiment where only a small volume is optically pumped, which implies that the conventional optical confinement factor $\Gamma = \frac{V_\mathrm{a}}{V}$ should be modified, where V_a is the the active material volume and V is the laser cavity mode volume. The relevant parameters are collected in Table B.1. The mode volume V, the confinement factor Γ, and the generalized confinement factor Γ^G are defined as

$$V = \frac{\int \epsilon_\mathrm{r}(r)|E_\mathrm{c}(r)|^2 dr}{\epsilon_\mathrm{r}(r_0)|E_\mathrm{c}(r_0)|^2} \tag{B.3}$$

$$\Gamma = \frac{V_\mathrm{a}}{V} \tag{B.4}$$

$$\Gamma^G = 2\frac{\int_{V_\mathrm{a}^\mathrm{G}} \epsilon_\mathrm{r}(r)|E_\mathrm{c}(r)|^2 dr}{\int \epsilon_\mathrm{r}(r)|E_\mathrm{c}(r)|^2 dr} \tag{B.5}$$

where r_0 is the position of the anti-node of the cavity field, V is mode volume of the Anderson-localized laser mode, V_a is the active volume covered by the carriers after excitation and subsequent diffusion, and V_a^G is the overlap between the cavity mode and the active volume. In order to reduce the number of free fitting parameters, we simplify the expression of Γ^G by assuming that the cavity field is uniformly distributed spatially with the amplitude $|E_\mathrm{c}(r)|^2 = \frac{1}{2}|E_\mathrm{c}(r_0)|^2$ and $\epsilon_\mathrm{r}(r) = \epsilon_\mathrm{r}(r_0)$, leading to

$$\Gamma^\mathrm{G} = \frac{V_\mathrm{a}^\mathrm{G}}{V} \tag{B.6}$$

Table B.1: Fixed material parameters for the semiconductor laser rate equation

Surface recombination rate (A) $= 2.5 \times 10^9\ \mathrm{s}^{-1}$
Bimolecular recombination rate (B) $= 10^{-16}\ \mathrm{m}^3/\mathrm{s}$
Auger non-radiative recombination rate (C) $= 8 \times 10^{-41}\ \mathrm{m}^6/\mathrm{s}$
Transparency carrier density (N_{tr}) $= 10^{24}\ \mathrm{m}^{-3}$
Gain coefficient (G_0) $= 2.5 \times 10^5\ \mathrm{m}^{-1}$
Effective refraction index (n_eff)$= 2.8$

We estimate the overlap volume between the active region and the cavity mode, V_a^G, as follows. The size of the active area is determined by the excitation beam which is 1.5 μm in diameter (red area in Fig. B.1). Here the carrier diffusion is neglected given that the carrier lifetime is extremely short above the lasing threshold. We also assume the Anderson-localized modes to be confined along the waveguide by the effect of the 2D PC gap (blue area in Fig. 5). From this, we extract an total overlap length of 1.5 μm, given by the active area, and an overlap width of $2a\sin\frac{\pi}{3} - 2r = 458\,\text{nm}$ given by the width of the PCW. The overlap height is given by the total thickness of 10 QW layers ($5\text{nm} \times 10$). In summary, we estimate

$$V_{\text{a}}^{\text{G}} = 1500 \times 458 \times 50 \ (\text{nm}^3) \tag{B.7}$$

$$V_{\text{a}} = (\pi \times 750^2 - 14 \times \pi \times 100^2) \times 50 \ (\text{nm}^3) \tag{B.8}$$

Finally, we estimate a cavity mode length by dividing the mode volume obtained with the rate equation model by an effective transverse mode area A_{eff}. To calculate A_{eff}, we assume the Anderson-localized modes to be confined along the waveguide. The width of the cavity mode can be calculated from finite-difference time-domain simulations of a PCW without disorder and the thickness of the cavity mode is assumed to be the same as the membrane.

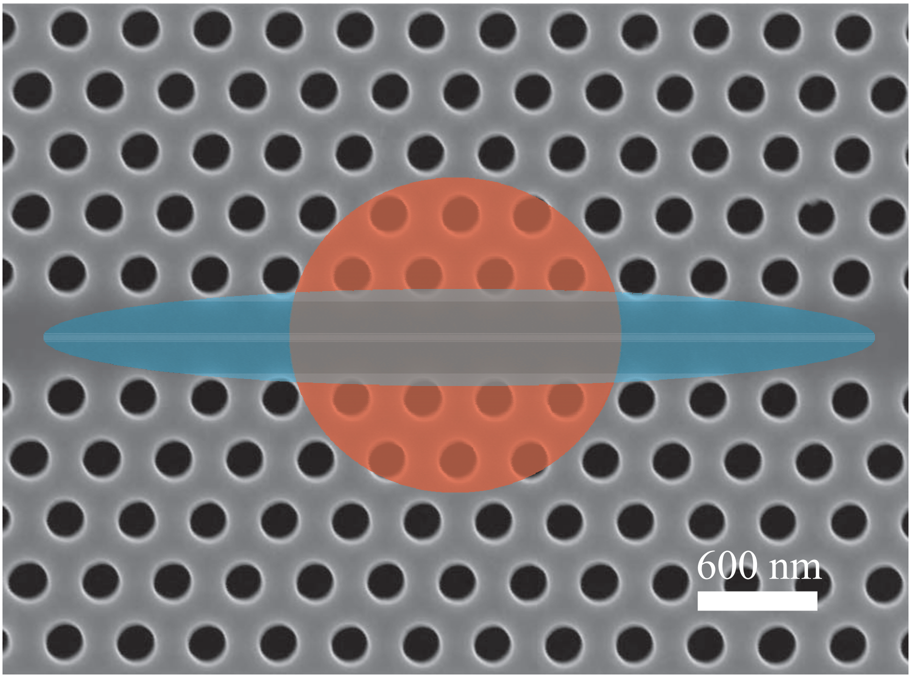

Figure B.1: (**The schematic illustration of the active area and cavity mode area.** The red area indicates the active area, related to V_a, and the blue area represents the area of a random laser mode, related to V. The overlap between both gives the effective active overlap which is related to V_{a}^{G}.

Averaging over one unit cell along the waveguide, we obtain a value of $\mathrm{A}_{\mathrm{eff}} = 0.11\,\mu\mathrm{m}^2$.

Appendix C

Optical characterization setup

The experimental setup used for characterizing the quantum dots emission in cryogenic temperature is sketched in Fig. C.1. It consists of excitation part, cryostat and the detection part. The excitation pulses are provided by a tunable Ti-sapphire laser (Coherent Mira 900) working in pico-modes with a repetition rate of 76 MHz. The laser can be tuned from 800 nm to 950 nm with a pulse duration of 2 ps. The sample sits on a cold finger in a Helium flow cryostat (Oxford Microstat HiRes II). A stable temperature between 4.2 K and 300 K can be obtained with a temperature controller which controls both a heater underneath the sample and the helium flow into the cryostat. A long working distance objective (Nikon LWD 40xC, NA = 0.65) is used for both exciting the QDs and collecting the QD emission. In order to minimize the scattered laser light, two long pass filter with cut off at 850nm and 875 nm have been used. Instead of using a pinhole, a single-mode polarization maintained fiber has been used to isolate the emission from single QDs. In the detection part, a monochromator (Princeton Instrument, SP2750) equipped with silicon charge-coupled devices (CCD) and AN avalanche photon diode (APD) is used to measure both the spectrum and lifetime of QDs. For the lifetime measurements, the quantum dots are repeatedly excited and the arrival times of single photon to the APD are correlated to the laser pulse by using a time correlator (Picoquant, Picoharp 300) with a resolution of 4 ps. By constructing a histogram of the delay

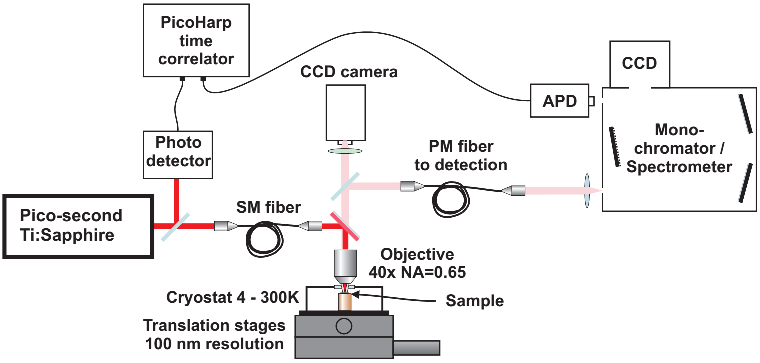
PicoHarp
time
correlator
CCD camera
CCD
APD
Mono-
chromator /
Spectrometer
Photo
detector
PM fiber
to detection
Pico-second
Ti:Sapphire
SM fiber
Objective
40x NA=0.65
Cryostat 4 - 300K
Sample
Translation stages
100 nm resolution

Figure C.1: Sketch of the experimental setup used for measuring the spectrum and lifetime of QDs.

between the arrive time of emitted photons and laser pulses, decay curves of QDs are obtained and can be fitted with either double- or single- exponential decay functions.

The random lasing measurements are performed with a similar confocal micro-photoluminescence setup where the silicon CCD is replaced by a cryogenically cooled InGaAs CCD. The InGaAs detector is cooled down by using liquid Nitrogen to reduce the dark counts.

Bibliography

[1] E. Purcell, H. Torrey and R. Pound. *Resonance Absorption by Nuclear Magnetic Moments in a Solid.* Physical Review **69**, 37 (1946).

[2] J. M. Gérard, B. Sermage, B. Gayral, B. Legrand, E. Costard *et al. Enhanced Spontaneous Emission by Quantum Boxes in a Monolithic Optical Microcavity.* Phys. Rev. Lett. **81**, 1110 (1998).

[3] W. Fang, J. Y. Xu, A. Yamilov, H. Cao, Y. Ma *et al. Large enhancement of spontaneous emission rates of InAs quantum dots in GaAs microdisks.* Optics Letters **27**, 948 (2002).

[4] P. Lodahl, A. Floris Van Driel, I. S. Nikolaev, A. Irman, K. Overgaag *et al. Controlling the dynamics of spontaneous emission from quantum dots by photonic crystals.* Nature **430**, 654 (2004).

[5] D. Englund, D. Fattal, E. Waks, G. Solomon, B. Zhang *et al. Controlling the Spontaneous Emission Rate of Single Quantum Dots in a Two-Dimensional Photonic Crystal.* Phys. Rev. Lett. **95**, 013904 (2005).

[6] S. Noda, M. Fujita and T. Asano. *Spontaneous-emission control by photonic crystals and nanocavities.* Nature Photonics **1**, 449 (2007).

[7] D. S. Wiersma, P. Bartolini, A. Lagendijk and R. Righini. *Localization of light in a disordered medium.* Nature **390**, 671 (1997).

[8] T. J. Kippenberg and K. J. Vahala. *Cavity optomechanics: back-action at the mesoscale.* Science (New York, N.Y.) **321**, 1172 (2008).

[9] J. Zi. *Coloration strategies in peacock feathers.* Proceedings of the National Academy of Sciences **100**, 12576 (2003).

[10] E. Yablonovitch. *Inhibited Spontaneous Emission in Solid-State Physics and Electronics*. Physical Review Letters **58**, 2059 (1987).

[11] S. John. *Strong localization of photons in certain disordered dielectric superlattices*. Physical Review Letters **58**, 2486 (1987).

[12] T. Tanabe, M. Notomi, E. Kuramochi, A. Shinya and H. Taniyama. *Trapping and delaying photons for one nanosecond in an ultrasmall high-Q photonic-crystal nanocavity*. Nature Photonics **1**, 49 (2007).

[13] A. G. Baca, C. I. H. Ashby and I. o. E. Engineers. *Fabrication of GaAs Devices* (IET, 2005).

[14] K. J. Hennessy. *High-Q photonic crystal cavities with embedded quantum dots*. Proceedings of SPIE **5359**, 210 (2004).

[15] K. J. Hennessy. *Photonic Crystal Nanocavities Positioned and Tuned For Cavity-QED* (University of California Santa Barbara, 2006).

[16] E. Yablonovitch, T. Gmitter, J. P. Harbison and R. Bhat. *Extreme selectivity in the lift-off of epitaxial GaAs films*. Applied Physics Letters **51**, 2222 (1987).

[17] W. I. Jang, C. A. Choi, M. L. Lee, C. H. Jun and Y. T. Kim. *Fabrication of MEMS devices by using anhydrous HF gas-phase etching with alcoholic vapor*. Journal of Micromechanics and Microengineering **12**, 297 (2002).

[18] U. K. Khankhoje, S.-H. Kim, B. C. Richards, J. Hendrickson, J. Sweet *et al. Modelling and fabrication of GaAs photonic-crystal cavities for cavity quantum electrodynamics*. Nanotechnology **21**, 065202 (2010).

[19] S. Chu. *Laser Manipulation of Atoms and Particles*. Science **253**, 861 (1991).

[20] V. B. Braginsky and A. B. Manukin. *Measurement of Weak Forces in Physics Experiments* (University of Chicago Press, 1977).

[21] G. Anetsberger, R. Rivière, A. Schliesser, O. Arcizet and T. J. Kippenberg. *Ultralow-dissipation optomechanical resonators on a chip*. Nature Photonics **2**, 627 (2008).

[22] T. Kippenberg, H. Rokhsari, T. Carmon, A. Scherer and K. Vahala. *Analysis of Radiation-Pressure Induced Mechanical Oscillation of an Optical Microcavity.* Physical Review Letters **95** (2005).

[23] J. D. Teufel, T. Donner, D. Li, J. W. Harlow, M. S. Allman *et al. Sideband cooling of micromechanical motion to the quantum ground state.* Nature **475**, 359 (2011).

[24] J. Chan, T. P. M. Alegre, A. H. Safavi-Naeini, J. T. Hill, A. Krause *et al. Laser cooling of a nanomechanical oscillator into its quantum ground state.* Nature **478**, 89 (2011).

[25] H. Ukita, Y. Uenishi and H. Tanaka. *A Photomicrodynamic System with a Mechanical Resonator Monolithically Integrated with Laser Diodes on Gallium Arsenide.* Science **260**, 786 (1993).

[26] S. C. Masmanidis, R. B. Karabalin, I. De Vlaminck, G. Borghs, M. R. Freeman *et al. Multifunctional nanomechanical systems via tunably coupled piezoelectric actuation.* Science (New York, N.Y.) **317**, 780 (2007).

[27] M. Sheik-Bahae and R. I. Epstein. *Optical refrigeration.* Nature Photonics **1**, 693 (2007).

[28] K. Hennessy, A. Badolato, M. Winger, D. Gerace, M. Atatüre *et al. Quantum nature of a strongly coupled single quantum dot-cavity system.* Nature **445**, 896 (2007).

[29] G. D. Cole, S. Groblacher, K. Gugler, S. Gigan and M. Aspelmeyer. *Monocrystalline AlGaAs heterostructures for high-reflectivity high-Q micromechanical resonators in the megahertz regime.* Applied Physics Letters **92**, 261108 (2008).

[30] G. D. Cole, Y. Bai, M. Aspelmeyer and E. A. Fitzgerald. *Free-standing AlGaAs heterostructures by gas-phase etching of germanium.* Applied Physics Letters **96**, 261102 (2010).

[31] H. Yamaguchi, K. Kato, Y. Nakai, K. Onomitsu, S. Warisawa *et al. Improved resonance characteristics of GaAs beam resonators by epitaxially induced strain.* Applied Physics Letters **92**, 251913 (2008).

[32] L. Midolo, P. J. van Veldhoven, M. A. Dundar, R. Notzel and A. Fiore. *Electromechanical wavelength tuning of double-membrane photonic crystal cavities.* Applied Physics Letters **98**, 211120 (2011).

[33] L. Ding, C. Baker, P. Senellart, A. Lemaitre, S. Ducci *et al. High Frequency GaAs Nano-Optomechanical Disk Resonator*. Physical Review Letters **105** (2010).

[34] L. Ding, C. Baker, P. Senellart, A. Lemaitre, S. Ducci *et al. Wavelength-sized GaAs optomechanical resonators with gigahertz frequency*. Applied Physics Letters **98**, 113108 (2011).

[35] E. Gavartin, R. Braive, I. Sagnes, O. Arcizet, A. Beveratos *et al. Optomechanical Coupling in a Two-Dimensional Photonic Crystal Defect Cavity*. Physical Review Letters **106** (2011).

[36] J.-H. Kim. *Selective etching of AlGaAs/GaAs structures using the solutions of citric acid/*H_2O_2 *and de-ionized* H_2O*/buffered oxide etch.* Journal of Vacuum Science & Technology B: Microelectronics and Nanometer Structures **16**, 558 (1998).

[37] K. Usami, A. Naesby, T. Bagci, B. Melholt Nielsen, J. Liu *et al. Optical cavity cooling of mechanical modes of a semiconductor nanomembrane*. Nature Physics **8**, 168 (2012).

[38] D. Wilson, C. Regal, S. Papp and H. Kimble. *Cavity Optomechanics with Stoichiometric SiN Films.* Physical Review Letters **103** (2009).

[39] K. Hjort, F. Ericson, J.-A. Schweitz, C. Hallin and E. Janzén. *Hardness, internal stress and fracture toughness of epitaxial AlGaAs films*. Thin Solid Films **250**, 157 (1994).

[40] D. K. Gramotnev and S. I. Bozhevolnyi. *Plasmonics beyond the diffraction limit.* Nature Photonics **4**, 83 (2010).

[41] D. Chang, A. Sørensen, P. Hemmer and M. Lukin. *Quantum Optics with Surface Plasmons.* Physical Review Letters **97** (2006).

[42] D. E. Chang, A. S. Sørensen, E. A. Demler and M. D. Lukin. *A single-photon transistor using nanoscale surface plasmons*. Nature Physics **3**, 807 (2007).

[43] A. Dousse, L. Lanco, J. Suffczyński, E. Semenova, A. Miard *et al. Controlled Light-Matter Coupling for a Single Quantum Dot Embedded in a Pillar Microcavity Using Far-Field Optical Lithography*. Physical Review Letters **101** (2008).

[44] I. Wilson-Rae, P. Zoller and A. Imamoglu. *Laser Cooling of a Nanomechanical Resonator Mode to its Quantum Ground State*. Physical Review Letters **92** (2004).

[45] T. P. M. Alegre, A. Safavi-Naeini, M. Winger and O. Painter. *Quasi-two-dimensional optomechanical crystals with a complete phononic bandgap*. Optics Express **19**, 5658 (2011).

[46] E. Jaynes and F. Cummings. *Comparison of quantum and semiclassical radiation theories with application to the beam maser*. Proceedings of the IEEE **51**, 89 (1963).

[47] Y. Akahane, T. Asano, B.-S. Song and S. Noda. *High-Q photonic nanocavity in a two-dimensional photonic crystal.* Nature **425**, 944 (2003).

[48] C. C. Gerry and P. L. Knight. *Introductory Quantum Optics* (Cambridge University Press, 2005).

[49] S. M. Tan. *A computational toolbox for quantum and atomic optics*. Journal of Optics B: Quantum and Semiclassical Optics **1**, 424 (1999).

[50] G. Lindblad. *On the generators of quantum dynamical semigroups*. Communications in Mathematical Physics (1965-1997) **48**, 119 (1976).

[51] G. Björk, A. Karlsson and Y. Yamamoto. *Definition of a laser threshold.* Physical Review A **50**, 1675 (1994).

[52] Y. Mu and C. Savage. *One-atom lasers.* Physical Review A **46**, 5944 (1992).

[53] R. Herrmann, T. Sünner, T. Hein, A. Löffler, M. Kamp *et al. Ultrahigh-quality photonic crystal cavity in GaAs*. Optics Letters **31**, 1229 (2006).

[54] a. Auffèves, D. Gerace, J.-M. Gérard, M. Santos, L. Andreani *et al. Controlling the dynamics of a coupled atom-cavity system by pure dephasing*. Physical Review B **81**, 1 (2010).

[55] S. Fan, P. Villeneuve, J. Joannopoulos and E. Schubert. *High Extraction Efficiency of Spontaneous Emission from Slabs of Photonic Crystals.* Physical Review Letters **78**, 3294 (1997).

[56] M. Kaniber, A. Laucht, T. Hürlimann, M. Bichler, R. Meyer *et al. Highly efficient single-photon emission from single quantum dots within a two-dimensional photonic band-gap.* Physical Review B **77** (2008).

[57] K. H. Madsen, P. Kaer, A. Kreiner-Mø ller, S. Stobbe, A. Nysteen *et al. Non-Markovian phonon dephasing of a quantum dot probed by cavity quantum electrodynamics.* arXiv p. 5 (2012).

[58] S. Strauf and F. Jahnke. *Single quantum dot nanolaser.* Laser & Photonics Reviews pp. 607–633 (2011).

[59] M. Nomura, S. Iwamoto, M. Nishioka, S. Ishida and Y. Arakawa. *Highly efficient optical pumping of photonic crystal nanocavity lasers using cavity resonant excitation.* Applied Physics Letters **89**, 161111 (2006).

[60] M. Kaniber, A. Neumann, A. Laucht, M. F. Huck, M. Bichler *et al. Efficient and selective cavity-resonant excitation for single photon generation.* New Journal of Physics **11**, 013031 (2009).

[61] S. Strauf, K. Hennessy, M. Rakher, Y.-S. Choi, A. Badolato *et al. Self-Tuned Quantum Dot Gain in Photonic Crystal Lasers.* Physical Review Letters **96** (2006).

[62] M. Nomura, N. Kumagai, S. Iwamoto, Y. Ota and Y. Arakawa. *Photonic crystal nanocavity laser with a single quantum dot gain.* Optics Express **17**, 15975 (2009).

[63] C. Gies, J. Wiersig, M. Lorke and F. Jahnke. *Semiconductor model for quantum-dot-based microcavity lasers.* Physical Review A **75** (2007).

[64] S. Smolka, H. Thyrrestrup, L. Sapienza, T. B. Lehmann, K. R. Rix *et al. Probing the statistical properties of Anderson localization with quantum emitters.* New Journal of Physics **13**, 063044 (2011).

[65] P. W. Anderson. *Absence of Diffusion in Certain Random Lattices.* Physical Review **109**, 1492 (1958).

[66] H. Hu, A. Strybulevych, J. H. Page, S. E. Skipetrov and B. A. van Tiggelen. *Localization of ultrasound in a three-dimensional elastic network.* Nature Physics **4**, 945 (2008).

[67] J. Billy, V. Josse, Z. Zuo, A. Bernard, B. Hambrecht *et al. Direct observation of Anderson localization of matter waves in a controlled disorder.* Nature **453**, 891 (2008).

[68] K. J. Vahala. *Optical microcavities.* Nature **424**, 839 (2003).

[69] B. Redding, M. A. Choma and H. Cao. *Speckle-free laser imaging using random laser illumination.* Nature Photonics **6** (2012).

[70] Q. Song, S. Xiao, Z. Xu, V. M. Shalaev and Y. L. Kim. *Random laser spectroscopy for nanoscale perturbation sensing.* Optics letters **35**, 2624 (2010).

[71] V. S. Letokhov. *Generation of Light by a Scattering Medium with Negative Resonance Absorption.* Soviet Journal of Experimental and Theoretical Physics **26**, 835 (1968).

[72] N. M. Lawandy, R. M. Balachandran, A. S. L. Gomes and E. Sauvain. *Laser action in strongly scattering media.* Nature **368**, 436 (1994).

[73] J. Topolancik, B. Ilic and F. Vollmer. *Experimental Observation of Strong Photon Localization in Disordered Photonic Crystal Waveguides.* Physical Review Letters **99** (2007).

[74] L. Sapienza, H. Thyrrestrup, S. r. Stobbe, P. D. Garcia, S. Smolka *et al. Cavity quantum electrodynamics with Anderson-localized modes.* Science **327**, 1352 (2010).

[75] P. García, S. Smolka, S. Stobbe and P. Lodahl. *Density of states controls Anderson localization in disordered photonic crystal waveguides.* Physical Review B **82** (2010).

[76] S. Gottardo, R. Sapienza, P. D. García, A. Blanco, D. S. Wiersma *et al. Resonance-driven random lasing.* Nature Photonics **2**, 429 (2008).

[77] R. G. S. El-Dardiry and A. Lagendijk. *Tuning random lasers by engineered absorption.* Applied Physics Letters **98**, 161106 (2011).

[78] M. Leonetti, C. Conti and C. Lopez. *The mode-locking transition of random lasers.* Nature Photonics **5**, 615 (2011).

[79] H. Altug and J. Vuckovic. *Photonic crystal nanocavity array laser.* Optics Express **13**, 8819 (2005).

[80] V. Apalkov and M. Raikh. *Universal fluctuations of the random lasing threshold in a sample of a finite area.* Physical Review B **71** (2005).

[81] A. Tulek, R. C. Polson and Z. V. Vardeny. *Naturally occurring resonators in random lasing of π-conjugated polymer films.* Nature Physics **6**, 303 (2010).

[82] L. A. Coldren and S. W. Corzine. *Diode Lasers and Photonic Integrated Circuits* (Wiley-Interscience, 1995).

[83] T. Suhr, N. Gregersen, K. Yvind and J. Mø rk. *Modulation response of nanoLEDs and nanolasers exploiting Purcell enhanced spontaneous emission.* Optics Express **18**, 11230 (2010).

[84] A. Mock. *First principles derivation of microcavity semiconductor laser threshold condition and its application to FDTD active cavity modeling.* Journal of the Optical Society of America B **27**, 2262 (2010).

[85] M. Loncar, T. Yoshie, A. Scherer, P. Gogna and Y. Qiu. *Low-threshold photonic crystal laser.* Applied Physics Letters **81**, 2680 (2002).

[86] H. Thyrrestrup, S. Smolka, L. Sapienza and P. Lodahl. *Statistical Theory of a Quantum Emitter Strongly Coupled to Anderson-Localized Modes.* Physical Review Letters **108** (2012).

[87] A. Chabanov, M. Stoytchev and A. Genack. *Statistical signatures of photon localization.* Nature **404**, 850 (2000).

[88] S. Smolka. *Quantum Correlations and Light Localization in Disordered Nanophotonic Structures* (Technical University of Denmark, 2010).

Copyright: Jin Liu
and DTU Fotonik
All rights reserved
ISBN: 87-92062-84-9

Published by:
DTU Fotonik
Department of Photonics Engineering
Technical University of Denmark
Ørsteds Plads, building 343
DK-2800 Kgs. Lyngby

Jin Liu was born on 17th March, 1984, China. He received his B.Sc. and M.Sc. degrees in department of optoelectronics, South China Normal University in 2007 and 2009 respectively. The master's thesis was concerned with optical trapping and manipulation of nano- and micro-particles and its device applications.

During his Ph.D. study, Jin Liu was working on solid-state quantum photonics by using semiconductor quantum dots in photonic crystal membranes. He involved mainly in nanofabrication, optical characterization and modelling. This thesis was successfully defended on 19th September, 2012.

DTU Fotonik
Department of Photonics Engineering